

Model the nonlinear instability of wall-bounded shear flows as a rare event: a study on two-dimensional Poiseuille flow

Xiaoliang Wan^{1,4}, Haijun Yu² and E Weinan³

¹ Department of Mathematics, Louisiana State University, Baton Rouge, LA 70803, USA

² Institute of Computational Mathematics, Academy of Mathematics and Systems Science, Beijing 100190, People's Republic of China

³ Department of Mathematics and Program in Applied and Computational Mathematics, Princeton University, Princeton, NJ 08544, USA

E-mail: xlwan@math.lsu.edu, hyu@lsec.cc.ac.cn and weinan@math.princeton.edu

Received 23 May 2014, revised 23 February 2015

Accepted for publication 18 March 2015

Published 17 April 2015

Recommended by B Eckhardt



CrossMark

Abstract

In this work, we study the nonlinear instability of two-dimensional (2D) wall-bounded shear flows from the large deviation point of view. The main idea is to consider the Navier–Stokes equations perturbed by small noise in force and then examine the noise-induced transitions between the two coexisting stable solutions due to the subcritical bifurcation. When the amplitude of the noise goes to zero, the Freidlin–Wentzell (F–W) theory of large deviations defines the most probable transition path in the phase space, which is the minimizer of the F–W action functional and characterizes the development of the nonlinear instability subject to small random perturbations. Based on such a transition path we can define a critical Reynolds number for the nonlinear instability in the probabilistic sense. Then the action-based stability theory is applied to study the 2D Poiseuille flow in a short channel.

Keywords: hydrodynamic stability, minimum action method, large deviation theory

Mathematics Subject Classification: 34F05, 60H15, 60H30, 82C26

⁴ Author to whom any correspondence should be addressed.

1. Introduction

Since the first controlled scientific experiment given by Reynolds in 1883, modern hydrodynamic stability theory has evolved for more than a century. Many remarkable accomplishments have been achieved in this long adventure, however the fundamental problem of transition to turbulence has not yielded its secrets completely. In this work, we link the Freidlin–Wentzell (F–W) theory of large deviations with the subcritical bifurcation in wall-bounded parallel shear flows to study the nonlinear stability in the probabilistic sense. As a starting point, we focus on the instability of the two coexisting stable solutions of the two-dimensional (2D) Poiseuille flow in a short channel for the Reynolds number $Re \in (Re_G, Re_L)$, where Re_G is the global critical number indicating the onset of a subcritical bifurcation and Re_L is the critical number given by the linear stability theory. Before a detailed introduction of our strategy, we first review briefly some classical stability theories for viscous incompressible flows, including linear stability theory, nonlinear stability theory and nonmodal stability theory, especially for Poiseuille flows, as well as some recent results on the study of edge states and minimal seeds.

1.1. Linear stability theory

In general, linear stability theory describes the flow behaviour involving infinitesimal disturbances superimposed on a base flow. Rayleigh (1880) developed a general linear stability theory for inviscid plane-parallel shear flows. Orr (1907) and Sommerfeld (1908) reformulated Rayleigh's theory for a viscous incompressible fluid.

The Orr–Sommerfeld (O–S) analysis assumes a base flow with the form

$$\mathbf{u}_b(\mathbf{x}) = V(y)\mathbf{e}_x, \quad (1)$$

where \mathbf{e}_x is a unit vector in the streamwise direction, i.e., x direction, and y is the wall-normal direction. \mathbf{u}_b is an exact solution of the Navier–Stokes (N–S) equations subject to a force term $f(\mathbf{x}) = -\nu V''(y)\mathbf{e}_x$. For Poiseuille flows, the force is given by a pressure gradient along the streamwise direction. Let the solution of the N–S equations be $\mathbf{u}_{\text{tot}} = \mathbf{u}_b + \mathbf{u}$ and $p_{\text{tot}} = p_b + p$, where (\mathbf{u}, p) indicates the disturbance to the base flow. In particular, the following form of three-dimensional (3D) disturbance is assumed

$$(\mathbf{u}, p) = (\hat{\mathbf{u}}(y), \hat{p}(y))\mathbf{e}^{i\alpha(x-ct)+\beta z}, \quad (2)$$

which corresponds to a travelling wave in x direction. Here z indicates the spanwise direction. Then the linearized equations for \mathbf{u} and p can be manipulated to yield a single equation, i.e., the celebrated O–S equation, for the y -component velocity \hat{v} ,

$$(V - c)[\mathcal{D}^2 - k^2]\hat{v} - V''\hat{v} = \frac{1}{i\alpha Re}[\mathcal{D}^2 - k^2]^2\hat{v}, \quad (3)$$

where $\mathcal{D} = \frac{d}{dy}$, and $k = \sqrt{\alpha^2 + \beta^2}$ is the magnitude of the wave vector.

For wall-bounded shear flows, equation (3) represents an eigenvalue problem with homogeneous boundary conditions for a given base flow. The goal is then to find the dependence of c on Reynolds number and wave number. The O–S equation is exceedingly difficult to analyse for large Reynolds numbers when transition occurs. Many efforts have been directed to the asymptotic analysis to exploit the separation of length scales between the viscous layers and the flow macrostructure [1–5], until an accurate solution was obtained numerically [6]. According to the O–S theory, the plane Poiseuille flow is stable to infinitesimal disturbances for $Re < Re_L = 5772$ [6,7]. For each wave number α there is at most one unstable mode, with the eigenfunction symmetric (respectively, antisymmetric) about the centre line.

For very large Reynolds numbers, there are unstable modes only for a narrow band of wave numbers limited by the so-called lower and upper branches of the neutral stability curve.

1.2. Nonlinear stability theory

The linear stability theory of plane-parallel shear flows gives a description of the initial growth of very small disturbances, which is not able to yield a correct prediction about the transition. For example, the critical Reynolds number Re_L for wall-bounded shear flows such as Poiseuille flow, is much higher than the Reynolds number at which transition is observed in experiments. A natural argument for the discrepancy between linear theory and experiments is that the nonlinear effect of the disturbances has been neglected, which always exists as long as the amplitude of the perturbation is finite.

One approach to develop nonlinear stability theory is to expand the N–S equations in powers of the perturbation amplitude $A(t)$, i.e., the Stuart-Watson expansion [8, 9],

$$\frac{dA}{dt} = \sigma(Re, \alpha)A - \sum_{n=1}^N l_n(Re, \alpha)A^{2n+1}, \quad (4)$$

where N is the truncation order, $l_n(Re, \alpha)$ the Landau coefficients [10], and $\sigma(Re, \alpha)$ the linear growth rate of a wave at Reynolds number Re assumed close to the critical value for wave number α . In nonlinear stability theory, the Stuart-Watson expansion is frequently truncated at the lowest nontrivial order $N = 1$:

$$\frac{dA}{dt} = \sigma(Re, \alpha)A - l_1(Re, \alpha)A^3, \quad (5)$$

where the Landau coefficient l_1 plays a crucial role for the behaviour of the solution. If $l_1(Re, \alpha)$ is positive, a supercritical bifurcation occurs with respect to Re . If $l_1(Re, \alpha)$ is negative, the scenario is fundamentally different, where a subcritical bifurcation occurs. For the latter case, when $\sigma(Re, \alpha) < 0$, small disturbances with wave number α at Reynolds number Re decay subject to a threshold amplitude $A_0 = (\sigma/l_1)^{1/2}$, above which disturbances grow unboundedly. The point $A = A_0$ corresponds to an unstable finite-amplitude equilibrium. The difference from the linear stability theory is that although the growth rate is unbounded for linear unstable waves, there does not exist a threshold amplitude. The first Landau coefficient $l_1(Re, \alpha)$ for Poiseuille flow is negative for $Re < 6000$ [11, 12], which includes most of the range of interest for transition studies. Thus, Poiseuille flow is expected to have a subcritical bifurcation.

In principle, if the whole Stuart-Watson expansion is employed, the result should be an exact solution of the N–S equations. Based on such an observation, another approach in nonlinear stability theory is to seek numerically the solutions of the N–S equations [13–16]. The conclusion of these calculations is that there exists a nonlinear neutral surface in (Re, α, E) space, where E is the disturbance energy of the wave. For $E > 0$, there exist stable (upper-branch solutions) and unstable equilibria (lower-branch solutions) for certain combinations of Re and α . The nonlinear stability theory shows that the subcritical bifurcation occurs at a global critical number $Re_G \approx 2900$ [7, 14].

However, the analysis of steady equilibria does not provide a complete picture of the behaviour of arbitrary disturbances in Poiseuille flows. Nontrivial patterns without a well-defined period can be obtained. Secondary flows in a long channel were studied in [17], where equilibria with two or more characteristic length scales of variation were found at a Reynolds number smaller than 2900.

1.3. Nonmodal stability theory

Nonmodal stability theory defines a more appropriate measure of the disturbance size by taking into account the non-orthogonality of the eigenfunctions of the O–S operator \mathbf{L} . The maximum amplification $G(t)$ is defined as

$$G(t) = \max_{\mathbf{u}(0)} \frac{\|\mathbf{u}(t)\|_E^2}{\|\mathbf{u}(0)\|_E^2} = \max_{\mathbf{u}(0)} \frac{\|\exp(t\mathbf{L})\mathbf{u}(0)\|_E^2}{\|\mathbf{u}(0)\|_E^2} = \|\exp(t\mathbf{L})\|_E^2 \quad (6)$$

with respect to the energy norm for initial perturbations $\mathbf{u}(0)$. The operator norm $\|\exp(t\mathbf{L})\|_E$ can be characterized by the least stable mode of \mathbf{L} only when $t \rightarrow \infty$. For a finite time, the dynamics and spatial pattern selection can be significantly different due to the non-orthogonality of eigenmodes of \mathbf{L} . Thus a quantity to describe the energy growth for $t = 0^+$ is needed, which is given as [18–20]

$$\max_{\mathbf{u}} \frac{1}{\|\mathbf{u}\|_E^2} \left. \frac{d\|\mathbf{u}\|_E^2}{dt} \right|_{t=0^+} = \lambda_{\max}((\mathbf{L}^H + \mathbf{L})/2), \quad (7)$$

with $\lambda_{\max}(\cdot)$ being the largest eigenvalue. The quantity $\lambda_{\max}((\mathbf{L}^H + \mathbf{L})/2)$ is referred to as the numerical abscissa, which can be computed by determining the boundary of the numerical range of \mathbf{L} . It is observed that although all eigenvalues of \mathbf{L} may be confined to the stable half-plane, the numerical range can protrude into the unstable half-plane, which indicates that energy growth can be expected for small times. To describe the maximum transient energy growth on the complex plane, an extension of spectra, known as ε -pseudospectra can be introduced [20, 21] to measure the sensitivity of eigenvalues of \mathbf{L} with respect to a random perturbation of norm ε .

Evaluating the maximum transient growth $\max_{t>0} G(t)$ with respect to the streamwise wave number α and the Reynolds number Re , two important curves can be obtained. The first one is the familiar neutral curve given in the linear stability theory, which determines the critical Reynolds number $Re_L = 5772$; the other one separates parameter combinations for which the numerical range crosses into the unstable half-plane, which determines the critical Reynolds number $Re_E = 89$ given in the energy stability theory [22, 23]. For normal systems, the numerical range and the spectrum cross into the unstable half-plane at the same Reynolds number such that $Re_E = Re_L$. However, a wide gap may exist between Re_E and Re_L , which is characteristic of many non-normal fluid systems.

1.4. Edge states and minimal seeds

From aforementioned linear and nonlinear stability theories, we know that there are at least two locally stable solutions coexisting for a large range of Reynolds numbers. People are interested in how the transitions occur and evolve between the laminar state and the turbulence state. Then the boundary in the phase space separating the laminar state and the turbulent state needs to be understood, where any invariant structure, i.e., edge state [24], wrapped in the laminar-turbulent boundary [25], is particularly interesting. In [26], a saddle-like travelling wave was found on the laminar-turbulent boundary by a shooting and bisection method for a 3D channel flow. Later similar procedures were employed in [24, 27, 28] to study the laminar-turbulent boundary of the 3D Couette flow, Poiseuille flow and pipe flow, where the most interesting invariant set is the edge state defined by the edge of chaos [29].

To study how to effectively trigger the transition from laminar flow to turbulence, an optimization approach was adopted for a boundary-layer flow in [30], and for pipe flow in [31], to seek the minimal-energy perturbations, also called minimal seeds, that induce fast energy growth to a turbulent state within a sufficiently large time. This optimization approach was

quickly adopted to a more in-depth study on transitions in shear flows [32–35]. A survey of this optimization approach is given in [36].

1.5. Our strategy

We will focus on the scenario of subcritical bifurcation as in the nonlinear stability theory. In contrast to linear and nonmodal stability theories, we will work with the original N–S equations. The fundamental difference of our strategy from the deterministic stability theories is that we will introduce small noise into the force term and consider the long-term stochastic dynamics. Due to the existence of noise, transitions between the two coexisting stable solutions will eventually occur as long as the amplitude of the noise is finite. We are particularly interested in the case that the amplitude of the noise is small. According to the large deviation principle (LDP) given by the F–W theory, as the noise amplitude decreases to zero, the time required for the occurrence of transition will increase exponentially and the transition probability will decrease exponentially. Most importantly, the transition probability can be characterized in the asymptotic sense by the minimizer of the F–W action functional, which is also the most probable transition path or the minimal action path (MAP). Based on the MAP, we mainly ask the following two questions:

- (i) What is the relation between the Reynolds number and the relative transition probabilities of the two coexisting stable solutions?
- (ii) What information can the MAP reveal about the nonlinear instability of the stable solutions?

In this paper, we study these two questions using the 2D Poiseuille flow in a short channel as a starting point. More specifically, we examine the transitions between the base flow and the stable travelling wave solution by employing the minimum action method to seek numerically the MAPs. Based on the MAPs, we measure the metastability of the base flow and the travelling wave by comparing the actions required to escape their basins of attraction. A critical Reynolds number $Re_A \in (Re_G, Re_L)$ can be defined in the probabilistic sense, at which the transition probabilities between the base flow and the travelling wave are equal to each other in the asymptotic sense. We use a dynamic solver to examine the MAPs to figure out the transition states located on the separatrix, which are particularly important for the nonlinear instability. Due to the fact that the N–S equations correspond to a non-gradient system, the transition mechanism between the base flow and the travelling wave are of particular interest. We also note that the proposed strategy is not limited to the 2D Poiseuille flows but valid in general for subcritical bifurcations [37], which exist in many wall-bounded 2D and 3D parallel shear flows.

Our idea is also related to studies on edge states and minimal seeds. Instead of focusing on the structure of the separatrix, we are trying to measure the relative difficulties to move two stable states to the separatrix through random forcing. The LDP can also be applied to study small random perturbations in initial conditions. When the random initial perturbations are modelled by a Gaussian field, the LDP provides a weighted norm linking the covariance to the energy of the noise. Such a norm can be regarded as a generalization of the similar norm used for minimal seeds. Since we do not focus on random initial perturbations in this work, we outline the connection between LDP and minimal seeds in appendix A.

The paper is organized as follows. In section 2, we define the problem. The metastability is discussed in section 3. A brief description of numerical tools used in this paper is given in section 4. We present, in section 5, a detailed discussion about the transitions of the 2D Poiseuille flow in a short channel. Finally, a summary section 6 is given.

2. Problem description

We consider the following stochastic N–S perturbation equations for 2D Poiseuille flow defined on the physical domain $(x, y) \in D = [0, L] \times [-1, 1]$:

$$\begin{cases} \frac{\partial \mathbf{u}}{\partial t} + (\mathbf{u}_{\text{tot}} \cdot \nabla) \mathbf{u}_{\text{tot}} = -\nabla p + \frac{1}{Re} \Delta \mathbf{u} + \sqrt{\varepsilon} \dot{W}(t, \mathbf{x}), \\ \nabla \cdot \mathbf{u} = 0, \end{cases} \quad (8)$$

where x is the streamwise direction, y the wall-normal direction, L the length of the channel, Re the Reynolds number, \dot{W} divergence-free space-time white noise, and ε a small positive number. When $\varepsilon = 0$, system (8) becomes deterministic. We are interested in the case $0 < \varepsilon \ll 1$, i.e., the random perturbations are small. Equation (8) is obtained as follows. We let $\mathbf{u}_{\text{tot}} = \mathbf{u}_b + \mathbf{u}$ and $p_{\text{tot}} = p_b + p$, where \mathbf{u}_b and p_b are the velocity and pressure of the 2D Poiseuille flow respectively. Then \mathbf{u} and p indicate the deviation from the base flow. Substituting $\mathbf{u}_b = (1 - y^2, 0)$ and $p_b = -\frac{2}{Re}x$ into the original N-S equations, we obtain equation (8) as a simplification.

Consider the divergence-free space

$$H = \{\mathbf{u} \in L_2(D) | \nabla \cdot \mathbf{u} = 0, \mathbf{u} \cdot \mathbf{n}|_{y=\pm 1} = 0, \mathbf{u}|_{x=0} = \mathbf{u}|_{x=L}\}. \quad (9)$$

The Helmholtz–Hodge decomposition says that for a given \mathbf{u} there exists a unique p^* , such that

$$\text{NS}(\mathbf{u}, p) := -(\mathbf{u}_{\text{tot}} \cdot \nabla) \mathbf{u}_{\text{tot}} + \frac{1}{Re} \Delta \mathbf{u} - \nabla p$$

belongs to H when $p = p^*$. We write $\text{NS}(\mathbf{u}) = \text{NS}(\mathbf{u}, p^*)$ as the divergence-free part of the advection term and the diffusion term. Then the stochastic N–S equations are often written as the following stochastic evolution equation

$$d\mathbf{u} - \text{NS}(\mathbf{u}) dt = \sqrt{\varepsilon} dW(t), \quad (10)$$

where the Wiener process $W(t)$ takes its value in H . Since equation (10) is defined on a divergence-free space, the pressure disappears.

Remark 1. Equation (8) is an oversimplified model in the sense that we do not introduce a finite spatial correlation length in the noise. Since we focus on numerical studies in this work, we will only consider approximated white noise in a finite dimensional space given by the spatial discretization. The approximated white noise can be regarded as smooth noise in space subject to a correlation length that decreases as the spatial discretization is refined.

2.1. Nonlinear instability and subcritical bifurcation

In hydrodynamic stability theory, the commonly used stability criteria are essentially a one-direction measure of sensitivity of a solution to the N–S equations with respect to perturbations. The basic stability is defined as

$$\lim_{t \rightarrow \infty} \frac{E_V(t)}{E_V(0)} \rightarrow 0, \quad (11)$$

where $E_V(t)$ is the kinetic energy of the disturbance at time t in a volume V . If $E_V(t)$ goes to zero as $t \rightarrow \infty$, we say that the solution is stable to perturbations. If the stability depends on the energy of the initial perturbations, a conditional stability can be defined where the solution is only stable when $E_V(0)$ is smaller than a threshold energy $\delta > 0$. If $\delta \rightarrow \infty$, it corresponds to the global stability. Based on such a definition, the main effort is devoted to find out the critical Reynolds number such that the stability criterion (11) is satisfied, by measuring the

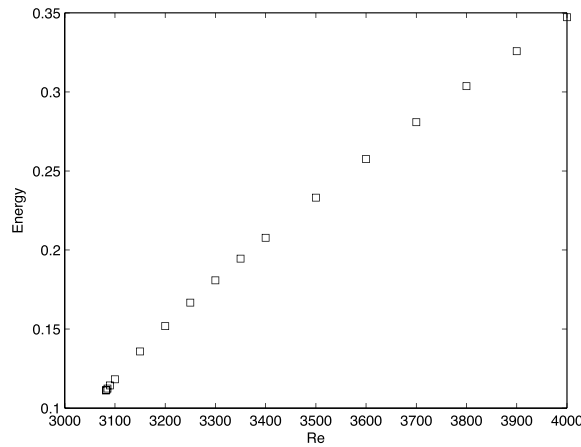


Figure 1. Energy of the upper-branch solutions of 2D Poiseuille flow for channel length $L = 5$ subject to Fourier modes $e^{\frac{i2\pi nx}{L}}$, $|n| \leq 4$, in the x direction and 32 Legendre modes in the y direction.

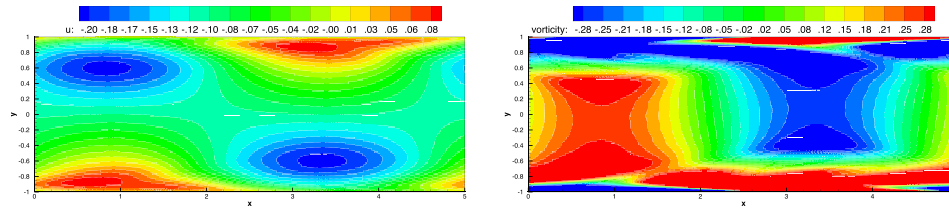


Figure 2. Snapshots of the upper-branch travelling wave solution at $Re = 3150$. Left: horizontal velocity; right: vorticity.

maximum growth rate of the disturbance. In the linear theory, the amplification of disturbances is characterized in terms of the least stable eigenvalue of the linearized N–S operator, e.g., the O–S operator. Since the linearized N–S operators often have a set of nonorthogonal eigenfunctions, the least stable mode is not enough for the quantitative prediction of energy growth for a finite time. In nonmodal stability theory, the growth rate of perturbations is measured by taking into account the aforementioned non-orthogonality. For example, the well-known critical Reynolds number predicted by the linear theory for 2D Poiseuille flow is $Re_L = 5772$ in contrast to $Re_E = 89$ given by the nonmodal stability theory or the energy theory, which indicates the largest Reynolds number below which the initial perturbation energy decays monotonically. For Reynolds numbers $Re \in (89, 5772)$, significant transition growth is expected. Such an interval includes the critical Reynolds number $Re_G \approx 2900$ given by the nonlinear stability theory, where the N–S equations are approximated numerically by searching a finite-amplitude travelling wave. In other words, we have a subcritical bifurcation in terms of the Reynolds number, where for $Re \in (Re_G, Re_L)$ there exists at least one different sustainable state from the base flow, see figures 1 and 2.

3. Nonlinear instability and LDP

When there exists small noise in force, it is necessary to consider *metastability*. The term metastability is used here rather loosely, since metastability is usually referred to for the

energy landscape of a gradient system while the N–S equations correspond to a non-gradient system. For simplicity and without loss of generality, we assume that there exist only two stable states for $Re \in (Re_G, Re_L)$: one is the base flow corresponding to a trivial solution \mathbf{u}_0 of equation (8) with $\varepsilon = 0$, the other one is a finite-amplitude travelling wave solution \mathbf{u}_+ . This scenario holds for the 2D Poiseuille flow when the channel length is relatively small. When the channel length becomes larger the sustainable stable solution may have a quasi-periodic form instead of a travelling wave [17].

For any $Re \in (Re_G, Re_L)$, there always exists a non-zero probability such that the noise can trigger a transition from \mathbf{u}_0 to \mathbf{u}_+ no matter how small the noise amplitude is. Then \mathbf{u}_0 loses its stability. However, once \mathbf{u}_+ is reached, it is also expected that the noise will trigger a transition from \mathbf{u}_+ back to \mathbf{u}_0 . Then the one-direction stability criterion (11) will break down. Instead, we need to consider the following bidirectional metastability:

$$\mathbf{u}_0 \xrightarrow{\kappa_{0 \rightarrow +}} \mathbf{u}_+ \xrightarrow{\kappa_{+ \rightarrow 0}} \mathbf{u}_0 \tag{12}$$

where $\kappa_{0 \rightarrow +}$ indicates the transition rate from \mathbf{u}_0 to \mathbf{u}_+ , and $\kappa_{+ \rightarrow 0}$ the transition rate from \mathbf{u}_+ to \mathbf{u}_0 . In other words, the stochastic dynamics under a small random force is characterized by a random walk between \mathbf{u}_0 and \mathbf{u}_+ . To this end, we have an overall picture for the stochastic dynamics: For $Re < Re_G$, \mathbf{u}_0 is globally stable; for $Re \in (Re_G, Re_L)$, both \mathbf{u}_0 and \mathbf{u}_+ are metastable; and for $Re > Re_L$, \mathbf{u}_+ is globally stable.

To measure the metastability of \mathbf{u}_0 and \mathbf{u}_+ , we resort to the F–W theory of large deviations. Let $\mathbf{u}(t, \mathbf{x})$ be an absolutely continuous function defined on $(t, \mathbf{x}) \in [0, T] \times D$, such that $\mathbf{u}(0, \mathbf{x}) = \mathbf{u}_0$ and $\mathbf{u}(T, \mathbf{x}) = \mathbf{u}_+$. We say such a function $\mathbf{u}(t, \mathbf{x})$ defines a transition trajectory from \mathbf{u}_0 to \mathbf{u}_+ on $[0, T]$. Let B be a set of random events, which contains all transition trajectories, i.e.,

$$B = \{\mathbf{u}(t, \mathbf{x}) | \mathbf{u}(t, \mathbf{x}) \text{ is a transition trajectory from } \mathbf{u}_0 \text{ to } \mathbf{u}_+ \text{ on } [0, T]\}. \tag{13}$$

The F–W theory [38, 39] gives the following LDP

$$V(\mathbf{u}_0, \mathbf{u}_+) := \lim_{T \rightarrow \infty} \lim_{\delta \downarrow 0} \lim_{\varepsilon \downarrow 0} [-\varepsilon \log \Pr(\tau_\delta \leq T)] = \inf_{T \in \mathbb{R}^+} \inf_{\mathbf{u} \in B} S_T(\mathbf{u}), \tag{14}$$

where $V(\mathbf{u}_0, \mathbf{u}_+)$ is called the quasi-potential from \mathbf{u}_0 to \mathbf{u}_+ , τ_δ indicates the first entrance time of the δ -neighbourhood of \mathbf{u}_+ for the trajectory starting from \mathbf{u}_0 , and $S_T(\mathbf{u})$ is the action functional defined as

$$S_T(\mathbf{u}) = \frac{1}{2} \int_0^T \|\partial_t \mathbf{u} - \mathbf{NS}(\mathbf{u})\|_2^2 dt, \tag{15}$$

Here $\|\cdot\|_2$ denotes the L_2 norm in physical space. Such a definition is consistent with the stochastic N-S equations in the evolution form (10) [38]. Simply speaking, the quasi-potential $V(\mathbf{u}_0, \mathbf{u}_+)$ measures the difficulties for the noise to move the state from \mathbf{u}_0 to \mathbf{u}_+ . In the current numerical implementations, we include the pressure p in the action functional and leave the Helmholtz–Hodge decomposition to the optimization problem induced by the quasi-potential, see (B.1) and [40].

The minimizer \mathbf{u}^* of the action functional is also called the ‘minimal action path’ (MAP), which is a deterministic path connecting \mathbf{u}_0 and \mathbf{u}_+ . The MAP is the most probable transition path because it requires the least action. Then the LDP says the transition rates between \mathbf{u}_0 and \mathbf{u}_+ satisfy in the asymptotic sense

$$\kappa_{0 \rightarrow +} \asymp e^{-\frac{V(\mathbf{u}_0, \mathbf{u}_+)}{\varepsilon}}, \quad \kappa_{+ \rightarrow 0} \asymp e^{-\frac{V(\mathbf{u}_+, \mathbf{u}_0)}{\varepsilon}} \tag{16}$$

where $f(\varepsilon) \asymp g(\varepsilon)$ if and only if $\log f(\varepsilon) / \log g(\varepsilon) \rightarrow 1$ as $\varepsilon \rightarrow 0$. This way, the quasi-potential provides a quantitative measure for the transitions between \mathbf{u}_0 and \mathbf{u}_+ in a probabilistic sense.

Let $\mathbf{u}_{0 \rightarrow +}$ indicate the MAP from \mathbf{u}_0 to \mathbf{u}_+ and $\mathbf{u}_{+ \rightarrow 0}$ the MAP from \mathbf{u}_+ to \mathbf{u}_0 . In the probabilistic sense, we say that \mathbf{u}_0 is more stable than \mathbf{u}_+ if the transition rate from \mathbf{u}_0 to \mathbf{u}_+ is smaller than that from \mathbf{u}_+ to \mathbf{u}_0 , i.e., $\kappa_{0 \rightarrow +} < \kappa_{+ \rightarrow 0}$. According to the LDP, it is much easier to work with the quasi-potential by noting that in the asymptotic sense

$$\kappa_{0 \rightarrow +} < \kappa_{+ \rightarrow 0} \Leftrightarrow V(\mathbf{u}_0, \mathbf{u}_+) > V(\mathbf{u}_+, \mathbf{u}_0). \quad (17)$$

In other words, the transition from \mathbf{u}_0 to \mathbf{u}_+ is less likely to occur if a larger action is needed. We then define a ratio [37]

$$r_{0 \leftrightarrow +} = \frac{V(\mathbf{u}_0, \mathbf{u}_+)}{V(\mathbf{u}_+, \mathbf{u}_0)}. \quad (18)$$

We say that \mathbf{u}_0 is more stable if $r_{0 \leftrightarrow +} > 1$, and \mathbf{u}_+ is more stable if $r_{0 \leftrightarrow +} < 1$.

From the physical point of view, the action functional depends on the Reynolds number. It is easy to see that there exist two limit cases. When $Re < Re_G$, the state \mathbf{u}_+ does not exist since \mathbf{u}_0 is globally stable. We can regard $V(\mathbf{u}_+, \mathbf{u}_0) = 0$, i.e., $r_{0 \leftrightarrow +} = \infty$. When $Re > Re_L$, \mathbf{u}_0 is linearly unstable. Then $V(\mathbf{u}_0, \mathbf{u}_+) = 0$, i.e., $r_{0 \leftrightarrow +} = 0$. From Re_G to Re_L , \mathbf{u}_0 becomes weaker, i.e., $V(\mathbf{u}_0, \mathbf{u}_+)$ decreases, and \mathbf{u}_+ becomes stronger, i.e., $V(\mathbf{u}_+, \mathbf{u}_0)$ increases. We then expect that $r_{0 \leftrightarrow +}$ is monotonically decreasing in terms of Re . If this holds, we can define a new critical Reynolds number Re_A , at which $r_{0 \leftrightarrow +} = 1$. In other words, in the asymptotic sense, the base flow is more stable for $Re \in (Re_G, Re_A)$ and less stable for $Re \in (Re_A, Re_L)$.

We have the following comments about the critical Reynolds number Re_A . First, Re_A is based on the stochastic dynamics instead of the deterministic dynamics. The stochastic dynamics can be more consistent with physical experiments since noise is ubiquitous in nature. Second, Re_A describes a long-term global phenomenon of the N–S equations perturbed by small noise, which naturally links the transition to the nonlinear instability of \mathbf{u}_0 and \mathbf{u}_+ . Third, Re_A is defined through quasi-potentials $V(\mathbf{u}_0, \mathbf{u}_+)$ and $V(\mathbf{u}_+, \mathbf{u}_0)$, which are characterized by the most probable transition path, i.e., the MAP. Due to the assumption of small noise, the MAP should be closely related to the structure of the phase space of the N–S equations.

To this end, we have established a connection between the nonlinear instability of the base flow and the F–W theory of large deviations by considering small noise in the force. Actually the LDP can also be employed to study small random perturbations in initial conditions, which yields another strategy to study the instability of the base flow. Since we focus on the former strategy in this paper, we outline the second strategy in appendix A.

Remark 2. The action functional (15) is, in general, defined for noise that is white in time and coloured in space from the point of view of stochastic partial differential equations [38] especially for a physical dimension more than one, where the norm in space should include the information about the correlation length l_c . Recent studies [41–43] show that under certain conditions, such as $0 < \varepsilon \ll l_c \ll 1$, the correlation length l_c can disappear at the level of large deviations, i.e., a regular L_2 norm in space can be used. If we consider numerical approximation with an approximated white noise, the above concern is, in general, not necessary, since the approximation space given by spatial discretization has a finite dimension.

4. Numerical tools

The key issue of applying the LDP to study the subcritical bifurcation is to solve the optimization problem induced by the quasi-potential (14). The main difficulty of solving this optimization problem is that the action functional may reach its (local) minimum at $T^* = \infty$, where T^*

is the optimal integration time, see equation (14). This case actually occurs for our problem because \mathbf{u}_0 is a fixed point.

We employ the high-order adaptive minimum action method (aMAM) [40, 44] designed particularly for $T^* = \infty$, where a moving mesh technique is used to deal with the scale separation between the fast and slow dynamics. A parallel version of this method was developed in [45]. We also need a MAM that is able to deal with a finite T^* , where we employ a recently developed MAM, called tMAM [46]. The main characteristics of tMAM include: (1) it inherits the high-order finite element approximation space used in [40] and the hybrid parallelization strategy developed in [45]; (2) it is able to deal with the transition between two arbitrary points in phase space; (3) it replaces the global reparametrization induced by the moving mesh technique with h -adaptivity, i.e., local refinement of finite elements. Since this is the first time that tMAM is applied to the N–S equations, we outline the algorithm in appendix B. We also provide a general discussion about our numerical strategy in appendix C to help clarify some numerical results, which will be referred to whenever necessary.

To study the obtained MAP, we also need a dynamic solver of the deterministic N–S equations. The details of the dynamic solver can be found in the appendix of [40].

5. Transitions of the 2D Poiseuille flow in a short channel

5.1. Problem setting

We take $L = 5$, and employ Fourier modes $e^{\frac{i2\pi nx}{L}}$, $|n| \leq 4$ for the physical discretization in x direction and 32 Legendre modes in y direction. Starting from $Re \approx 3080$, the stable upper-branch solutions emerge, which take a form of travelling wave. The energy of the upper-branch solutions is plotted in figure 1 versus the Reynolds number.

The reason that we choose such a coarse resolution is twofold: first, the MAM is computationally demanding and this is almost the coarsest resolution for a dynamic solver to capture the subcritical bifurcation; second, since the N–S equations correspond to a non-gradient system, the transition mechanism between the base flow and the upper-branch travelling wave solutions is not clear at all. We then want to use a coarse resolution as a starting point to identify the main physical phenomena and possible numerical issues for further algorithm refinement to study more realistic cases.

5.2. Transition from \mathbf{u}_0 to \mathbf{u}_+

We start with the Reynolds number $Re = 3150$. The initial state of the transition is \mathbf{u}_0 , which is a fixed point in the phase space. The upper-branch travelling wave solution \mathbf{u}_+ corresponds to a compact set of points in the phase space. We can choose one arbitrary point on the travelling wave as the final state, since any two points on the travelling wave are equivalent due to the fact that they are connected by a trajectory, which corresponds to a zero action [47]. Snapshots of the horizontal velocity and the vorticity of \mathbf{u}_+ are given in figure 2.

Let $\mathbf{u}_{0 \rightarrow +}(t)$ be the MAP from \mathbf{u}_0 to \mathbf{u}_+ given by the MAM. Let $U_{\hat{\mathbf{u}}(\mathbf{x})}(\tau)$ be a numerical trajectory given by the dynamic solver starting from the state $\hat{\mathbf{u}}(\mathbf{x})$. For clarity, we use t to indicate the time for the MAM and τ the time for the dynamic solver.

5.2.1. A typical transition scenario. Since only two stable solutions \mathbf{u}_0 and \mathbf{u}_+ coexist, the simplest possible transition scenario in the phase space is that there exists an unstable saddle-like solution \mathbf{u}_s , whose unstable manifolds connect with \mathbf{u}_0 and \mathbf{u}_+ and its stable manifolds form the separatrix between \mathbf{u}_0 and \mathbf{u}_+ . We know that such a mechanism is valid for a gradient

system, where the transition states are saddle points of index one. However for non-gradient systems, the transition mechanism is not definite. Since we have no a priori knowledge about how the MAP exits the basin of attraction of \mathbf{u}_0 , we assume at this moment that the transition from \mathbf{u}_0 to \mathbf{u}_+ is through an unstable solution \mathbf{u}_s directly or indirectly. Then the transition period of the MAP can be decomposed as: $[-\infty, \infty] = [-\infty, T_s) \cup T_s \cup (T_s, \infty]$. Using any state on the MAP $\mathbf{u}_{0 \rightarrow +}(t)$ as the initial condition, the dynamic solver should have the following convergence behaviour

$$\left. \begin{aligned} U_{\mathbf{u}_{0 \rightarrow +}(t)}(\tau) &\rightarrow \mathbf{u}_0, & t \in [-\infty, T_s) \\ U_{\mathbf{u}_{0 \rightarrow +}(t)}(\tau) &\rightarrow \mathbf{u}_s, & t = T_s \\ U_{\mathbf{u}_{0 \rightarrow +}(t)}(\tau) &\rightarrow \mathbf{u}_+, & t \in (T_s, \infty] \end{aligned} \right\} \text{as } \tau \rightarrow \infty. \tag{19}$$

We call T_s the transition time and $\mathbf{u}_{0 \rightarrow +}(T_s)$ the transition state. If $\mathbf{u}_{0 \rightarrow +}(T_s) = \mathbf{u}_s$, the MAP exits the basin of attraction of \mathbf{u}_0 from the unstable solution \mathbf{u}_s . For our problem, \mathbf{u}_s is an unstable travelling wave, corresponding to the lower-branch equilibrium. Since there exists dynamics between $\mathbf{u}_{0 \rightarrow +}(T_s)$ and \mathbf{u}_+ , which theoretically corresponds to a zero action, we have

$$S_T(\mathbf{u}_{0 \rightarrow +}) = \frac{1}{2} \int_{-\infty}^{\infty} \|\partial_t \mathbf{u}_{0 \rightarrow +} - \mathbf{NS}(\mathbf{u}_{0 \rightarrow +})\|_2^2 dt = \frac{1}{2} \int_{-\infty}^{T_s} \|\partial_t \mathbf{u}_{0 \rightarrow +} - \mathbf{NS}(\mathbf{u}_{0 \rightarrow +})\|_2^2 dt, \tag{20}$$

i.e., only $\mathbf{u}_{0 \rightarrow +}(t)$ with $t \in [-\infty, T_s)$ contributes to the action functional

5.2.2. Find the transition time using the edge tracking algorithm. We now consider the discretization of the F–W action functional. The physical discretization is the same as \mathbf{u}_+ given by the dynamic solver. Since \mathbf{u}_0 is a fixed point, the MAP from \mathbf{u}_0 to \mathbf{u}_+ corresponds to an optimal integration time $T^* = \infty$. We then choose a finite but large T for aMAM [44]. Considering that the scale of diffusion time is of $O(Re)$, we first consider the time interval $[0, T = 4 \times 10^3]$. In the time direction, we use $N_e = 768$ finite elements, where fifth-order polynomials are used in each element.

Once the MAP $\mathbf{u}_{0 \rightarrow +}(t)$ is computed, the transition time T_s is obtained as follows. Instead of looking for T_s directly, we try to find a small interval (T_L, T_R) such that $T_s \in (T_L, T_R)$, where $U_{\mathbf{u}_{0 \rightarrow +}(T_L)}(\tau)$ converges to \mathbf{u}_0 and $U_{\mathbf{u}_{0 \rightarrow +}(T_R)}(\tau)$ to \mathbf{u}_+ . Initially, we let $T_L = 0$ and $T_R = T$. We then use the dynamic solver to check the trajectory $U_{\mathbf{u}_{0 \rightarrow +}((T_L+T_R)/2)}(\tau)$. If $U_{\mathbf{u}_{0 \rightarrow +}((T_L+T_R)/2)}(\tau)$ goes to \mathbf{u}_0 , we let $T_L = \frac{T_L+T_R}{2}$; otherwise, we let $T_R = \frac{T_L+T_R}{2}$. The bisection strategy is implemented recursively to reduce the value of $|T_R - T_L|$. This procedure is similar to the edge tracking algorithm used in [24, 26–29] etc.

We find $T_s \in (T_L = 3941.11318743894, T_R = 3941.11318743895)$. Due to the fact that the dynamic solver can solve a modified N–S equations exactly, T_L and T_R can be tracked up to the machine accuracy, where \mathbf{u}_0 and \mathbf{u}_+ are regarded as the exact solutions of the modified N–S equations.

The main observation about $\mathbf{u}_{0 \rightarrow +}(t)$ is that $T - T_R \approx 60$, which implies that the part of MAP $\mathbf{u}_{0 \rightarrow +}(t)$ with $t \in [T_R, T]$ is not accurate. Theoretically, $\mathbf{u}_{0 \rightarrow +}(t)$, $t \in [T_R, T]$, should correspond to a trajectory converging to \mathbf{u}_+ , which has a zero action. Since the scale of the relaxation time is of $O(Re)$, which is much larger than $T - T_R \approx 60$, the MAP $\mathbf{u}_{0 \rightarrow +}(t)$, $t \in [T_R, T]$, does not follow a dynamical trajectory. Our initial guess is that it might be related to the truncation of the integration time from ∞ to a finite T . We then look at the convergence behaviour of the dynamic solver $U_{\mathbf{u}_{0 \rightarrow +}(t)}(\tau)$, $t = T_L, T_R$, which is shown in figure 3. It is seen that before diverging to \mathbf{u}_0 or \mathbf{u}_+ , both trajectories approach a state of constant energy. Furthermore, as the value $T_R - T_L$ becomes smaller, the divergence will occur at a later time. It is then reasonable to expect that such a state of constant energy actually corresponds to the unstable travelling wave \mathbf{u}_s .

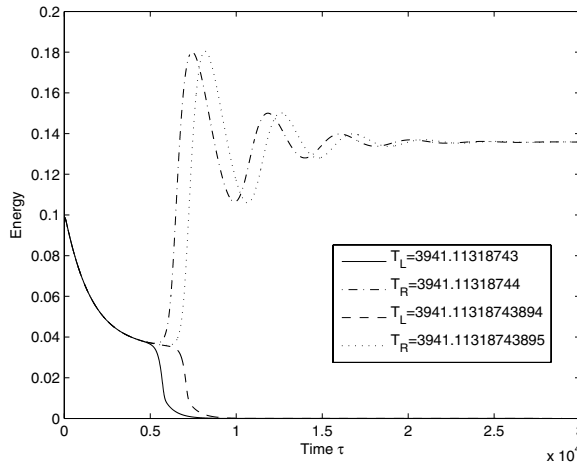


Figure 3. Energy evolution of of $U_{\mathbf{u}_0 \rightarrow +}(t)(\tau)$, $t = T_L, T_R$, i.e., the trajectories start from $\mathbf{u}_{0 \rightarrow +}(T_L)$ or $\mathbf{u}_{0 \rightarrow +}(T_R)$. The MAP $\mathbf{u}_{0 \rightarrow +}(t)$ is subject to integration time $T = 4 \times 10^3$. $Re = 3150$.

Although the dynamics from \mathbf{u}_s to \mathbf{u}_+ implies that no action is needed from \mathbf{u}_s to \mathbf{u}_+ , the discrepancy between the dynamic solver and the action functional in terms of the N–S operator (see appendix C) results in that a numerical trajectory will always have a non-zero action. This action is nothing but an approximation error, which is the accumulation of local residuals, defined in equation (C.5). Such a pollution is the reason that T_R is close to T . We will come back to this issue at the end of section 5.2.3 for a more detailed discussion.

5.2.3. Choose a new ending state. We then want to avoid approximating the trajectory in the basin of attraction of \mathbf{u}_+ . To do it, we consider the following strategy: instead of using \mathbf{u}_+ as the final state, we use \mathbf{u}_s since it is the only attractor on the separatrix.

We use $\mathbf{u}_{0 \rightarrow s}$ to denote the MAP from \mathbf{u}_0 to \mathbf{u}_s . Since we do not have an exact point on \mathbf{u}_s , we choose the state of the smallest energy on the trajectory $U_{\mathbf{u}_0 \rightarrow +}(T_R)(\tau)$ as the best available approximation of \mathbf{u}_s . Due to the fact that the N–S equations correspond to a non-gradient system, it is not necessary to reach a higher energy with a larger action. We choose this state only because we observe energy decay in figure 3 before the divergence occurs. We also double the total integration time from $T = 4 \times 10^3$ to $T = 8 \times 10^3$ to reduce the effect of truncation of the integration time and increase the number of elements to $N_e = 3072$. Since the final state is out of the basin of attraction of \mathbf{u}_0 , we can also define a transition time T_s as before.

For the MAP $\mathbf{u}_{0 \rightarrow s}$ given by $T = 8 \times 10^3$, we obtain $T_s \in (T_L = 7992.8775168529, T_R = 7992.8775168530)$. It is seen that the transition time T_s is much closer to T , which is what we expected. Due to the concern about convergence, we approximate \mathbf{u}_s again using $\mathbf{u}_{0 \rightarrow s}$ given by $T = 8 \times 10^3$ and compute the MAP using integration time $T = 1.6 \times 10^4$, where the element number N_e is also doubled. We then obtain $T_s \in (T_L = 15999.5389949618, T_R = 15999.5389949619)$. This implies that within the basin of attraction of \mathbf{u}_0 , the MAP goes directly to \mathbf{u}_s . The convergence behaviour of the dynamic solver $U_{\mathbf{u}_0 \rightarrow s}(t)(\tau)$, $t = T_L, T_R$, is given in figure 4. It is seen that the MAP $\mathbf{u}_{0 \rightarrow s}$ with $T = 8 \times 10^3$ provides a better approximation of \mathbf{u}_s compared to the MAP $\mathbf{u}_{0 \rightarrow +}$ with $T = 4 \times 10^3$.

To this end, we propose to use the action along the MAP $\mathbf{u}_{0 \rightarrow s}$ from $t = 0$ to $t = T_s$ as a better estimate of the minimum action required for the transition from \mathbf{u}_0 to \mathbf{u}_+ . Note here that

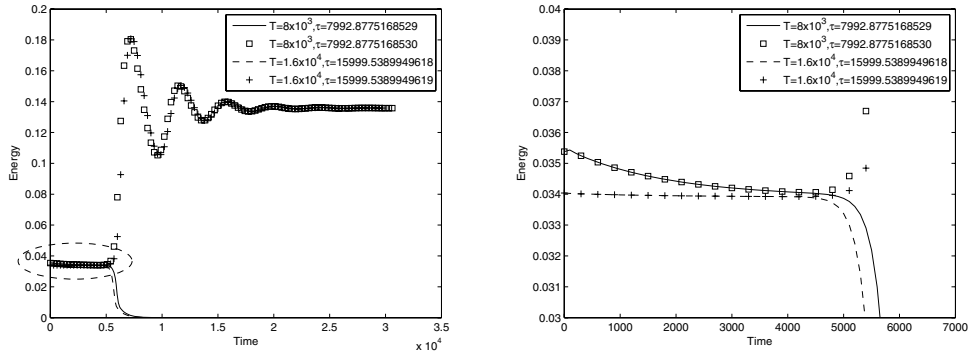


Figure 4. Left: convergence behaviour of a dynamic solver starting from $\mathbf{u}_{0 \rightarrow s}(T_L)$ and $\mathbf{u}_{0 \rightarrow s}(T_R)$, where the MAP $\mathbf{u}_{0 \rightarrow s}$ is computed with $T = 8 \times 10^3$, 1.6×10^4 . Right: the close-up view of the region marked by the ellipse in the left plot.

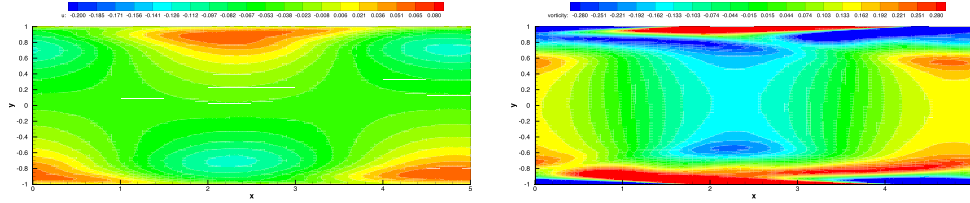


Figure 5. Snapshots of the approximate unstable solution \mathbf{u}_s . Left: horizontal velocity; right: vorticity.

the key is to obtain a good approximation of \mathbf{u}_s . To achieve this, we can iterate the following operations a few times if necessary:

- Use the current MAP $\mathbf{u}_{0 \rightarrow s}$ to obtain an approximation of \mathbf{u}_s .
- Compute the MAP $\mathbf{u}_{0 \rightarrow s}$ using the updated \mathbf{u}_s as the ending state.

In figure 5, we plot the approximated unstable travelling wave \mathbf{u}_s . It is seen that the contours are very similar with those of the stable travelling wave (see figure 2) except that \mathbf{u}_s has a much smaller energy, where the ratio $E_V(\mathbf{u}_s)/E_V(\mathbf{u}_+) \approx 25\%$.

We now go back to the issue that T_R is close to T when we compute the MAP using \mathbf{u}_+ as the final state. We compare the following two integrals given by local force (see equation (C.4)) and local residual (see equation (C.5))

$$\int_0^{T_s} \|F_{\mathbf{u}_{0 \rightarrow s}}(t, \mathbf{x})\|_2^2 dt \quad \text{and} \quad \int_0^{\hat{T}} \|R_{\mathbf{u}_{0 \rightarrow s}(T_R)}(\tau, \mathbf{x})\|_2^2 d\tau,$$

where \hat{T} is a number of order $O(Re)$ that is consistent with the convergence time of the dynamic solver. The first integral is nothing but the action from \mathbf{u}_0 to \mathbf{u}_s , which is equal to 1.31×10^{-5} . The second integral corresponds to the accumulated local residuals along the trajectory from \mathbf{u}_s to \mathbf{u}_+ . The energy of the trajectory $U_{\mathbf{u}_{0 \rightarrow s}(T_R)}(\tau)$ oscillates around the constant energy of \mathbf{u}_+ and such an oscillation decays gradually. The value of $\|R_{\mathbf{u}_{0 \rightarrow s}(T_R)}(\tau, \mathbf{x})\|_2^2$ is at least 1.3×10^{-7} and can be as high as $O(10^{-6})$ when the energy reaches its maximum. $\|R_{\mathbf{u}_{0 \rightarrow s}(T_R)}(\tau, \mathbf{x})\|_2^2$ is large because the high-order modes are important in the domain of attraction of \mathbf{u}_+ . Since the convergence time \hat{T} is of $O(Re)$, the second integral can be of $O(10^{-2})$. The difference between these two integrals can qualitatively explain why the MAP $\mathbf{u}_{0 \rightarrow +}$ picks a state which

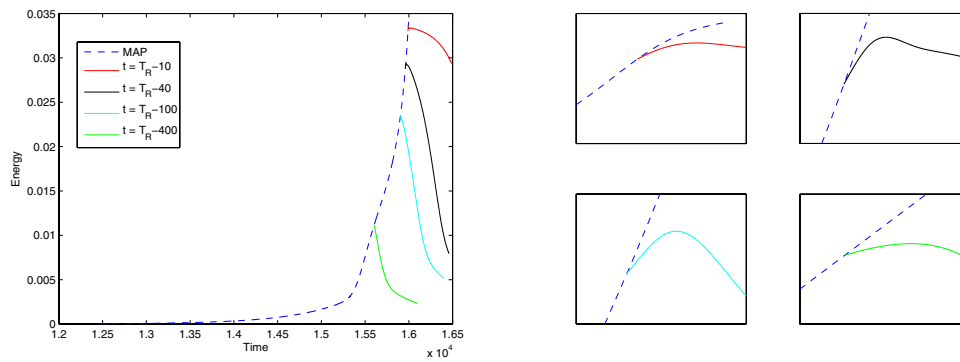


Figure 6. Left: energy evolution of MAP $\mathbf{u}_{0 \rightarrow s}$ and trajectories $U_{\mathbf{u}_{0 \rightarrow s}(t)}(\tau)$, where the MAP $\mathbf{u}_{0 \rightarrow s}$ is computed with $T = 1.6 \times 10^4$. t and τ share the horizontal axis. For the MAP, the horizontal axis indicates t ; for the trajectories $U_{\mathbf{u}_{0 \rightarrow s}(t)}(\tau)$, the horizontal axis indicate $t + \tau$ with a fixed t . Right: close-up view of the neighbourhood of $U_{\mathbf{u}_{0 \rightarrow s}(t)}(0)$.

is closer to the travelling wave to escape the domain of attraction of \mathbf{u}_0 such that T_R is close to T . It is a compromise between the action in the domain of attraction of \mathbf{u}_0 and the accumulated residuals in the domain of attraction of \mathbf{u}_+ along a numerical trajectory.

Remark 3. So far the numerical experiments show that if we can obtain a good approximation of \mathbf{u}_s , the transition time $T_s \approx T$ for the MAP $\mathbf{u}_{0 \rightarrow s}$. The most important observation in nonmodal theory is that the non-orthogonality of the eigenfunctions of the O–S operator can introduce significant energy growth at a finite time before the energy eventually decays. Then it is possible that $\mathbf{u}_{0 \rightarrow s}$ can first land onto the stable manifold of \mathbf{u}_s at a state of smaller energy than \mathbf{u}_s . However, for the current resolution, we did not observe this for different initial guesses we tested when computing $\mathbf{u}_{0 \rightarrow s}$.

5.2.4. How to use the action effectively. Numerical experiments show that the transition from \mathbf{u}_0 to \mathbf{u}_+ appears to pass through the unstable travelling wave \mathbf{u}_s . We now look at how the action is used to move the state from \mathbf{u}_0 to \mathbf{u}_s . In figure 6 we plot on the left the energy evolution of the MAP $\mathbf{u}_{0 \rightarrow s}$ and several trajectories $U_{\mathbf{u}_{0 \rightarrow s}(t)}(\tau)$, and provide on the right a close-up view of the neighbourhood of $U_{\mathbf{u}_{0 \rightarrow s}(t)}(0)$ for each sampled trajectory.

It is seen that along the MAP $\mathbf{u}_{0 \rightarrow s}$ the energy increases very slow before $t = 1.52 \times 10^3$, and then goes up very quickly until \mathbf{u}_s is reached. The four sampled initial states for the dynamic solver are all located in the basin of attraction of \mathbf{u}_0 , which means that their energy should eventually decay to zero. However, from the close-up view of the neighbourhood of $U_{\mathbf{u}_{0 \rightarrow s}(t)}(0)$, we see that the energy of $U_{\mathbf{u}_{0 \rightarrow s}(t)}(\tau)$ actually increases first before it starts to decay. This is consistent with the nonmodal stability theory, i.e., the non-orthogonal eigenfunctions of the O–S operator imply that perturbations may increase for a finite time although the state is linearly stable. The MAP obviously takes advantage of such a property. First, the MAP goes through the states that can induce energy growth at the beginning. Considering that trajectories need a zero action, the MAP uses such a strategy to save some action to reach a higher energy. Second, since all states within the basin of attraction of \mathbf{u}_0 eventually decay, the MAP then uses the action to ‘jump’ from one state to another one that can induce a higher energy and go closer to \mathbf{u}_s meanwhile.

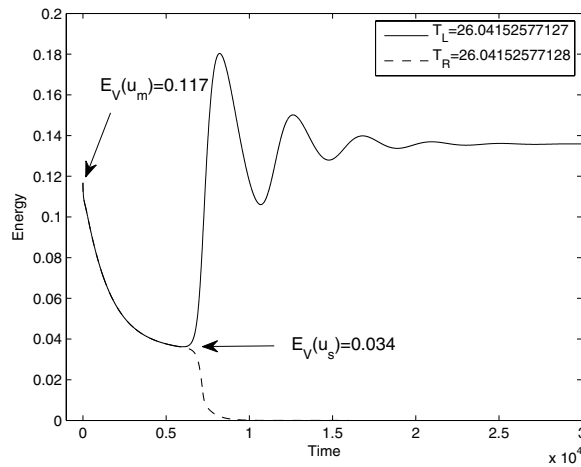


Figure 7. Energy evolution of of $U_{\mathbf{u}_+ \rightarrow 0}(t)(\tau)$, $t = T_L, T_R$, i.e., the trajectories start from $\mathbf{u}_+ \rightarrow 0(T_L)$ or $\mathbf{u}_+ \rightarrow 0(T_R)$. The MAP $\mathbf{u}_{0 \rightarrow +}(t)$ is subject to integration time $T = 1.6 \times 10^4$. $Re = 3150$.

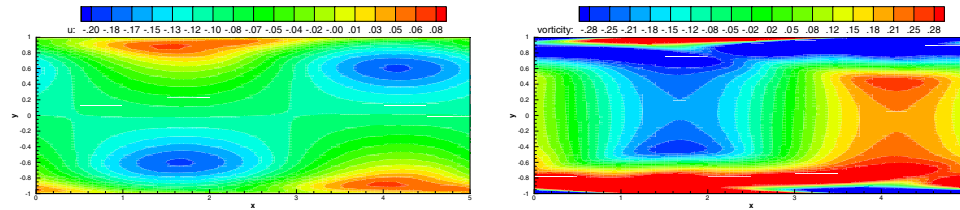


Figure 8. The transition state (\mathbf{u}_m) from \mathbf{u}_+ to \mathbf{u}_0 subject to $T = 1.6 \times 10^4$. Left: horizontal velocity; right: vorticity.

5.3. Transition from \mathbf{u}_+ to \mathbf{u}_0

We now look at the MAP $\mathbf{u}_+ \rightarrow 0$ for the transition from \mathbf{u}_+ to \mathbf{u}_0 , where the integration time is chosen as $T = 1.6 \times 10^4$ with $N_e = 6144$. We obtain $T_s \in (T_L = 26.9688, T_R = 26.9689)$. The convergence behaviour of the dynamic solver $U_{\mathbf{u}_+ \rightarrow 0}(t)(\tau)$, $t = T_L, T_R$, is plotted in figure 7. It is seen that the divergence also occurs at the unstable travelling wave \mathbf{u}_s . Furthermore, the following two observations are particularly interesting:

- (i) The ‘transition’ state is located on the stable manifold of \mathbf{u}_s with a much larger energy than \mathbf{u}_s . Let \mathbf{u}_m indicate this state. In contrast to $\mathbf{u}_{0 \rightarrow +}$, such a scenario is actually in favour of the transition from \mathbf{u}_+ to \mathbf{u}_0 . Since \mathbf{u}_m is close to \mathbf{u}_+ , it is possible that only a small action is needed for the transition from \mathbf{u}_+ to \mathbf{u}_m . Once \mathbf{u}_m is reached, there exists dynamics from \mathbf{u}_m to \mathbf{u}_s , and then to \mathbf{u}_0 , where no action is needed. The energy of \mathbf{u}_m and \mathbf{u}_s is included in figure 7. Snapshots of \mathbf{u}_m are given in figure 8, which appear to be very similar to those of \mathbf{u}_+ given in figure 2.
- (ii) Compared to the total integration time, the transition time $T_s \approx 27$ is very small. Then it appears that a finite time is needed to minimize the action functional from \mathbf{u}_+ to \mathbf{u}_m . Note here that the state \mathbf{u}_m should depend on the snapshot we take on \mathbf{u}_+ .

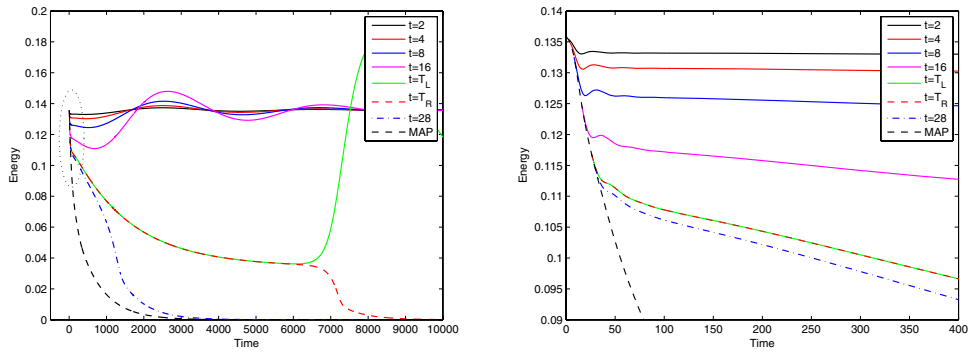


Figure 9. Left: energy evolution of MAP $\mathbf{u}_{+ \rightarrow 0}$ and trajectories $U_{\mathbf{u}_{+ \rightarrow 0}(t)}(\tau)$, where the MAP $\mathbf{u}_{+ \rightarrow 0}$ is computed with $T = 1.6 \times 10^4$. t and τ share the horizontal axis. For the MAP, the horizontal axis indicates t ; for the trajectories $U_{\mathbf{u}_{+ \rightarrow 0}(t)}(\tau)$, the horizontal axis indicates $t + \tau$ with a fixed t . Right: close-up view of the region marked by the eclipse in the left plot.

5.3.1. *Dynamical behaviour of $U_{\mathbf{u}_{+ \rightarrow 0}(t)}(\tau)$.* We sample a few points on the MAP $\mathbf{u}_{+ \rightarrow 0}(t)$ and look at the energy evolution of trajectories $U_{\mathbf{u}_{+ \rightarrow 0}(t)}(\tau)$, which is plotted figure 9 on the left, together with a close-up view on the right. For comparison, we also include the energy evolution along the MAP $\mathbf{u}_{+ \rightarrow 0}(t)$.

It is seen that the computed MAP $\mathbf{u}_{+ \rightarrow 0}(t) : \mathbf{u}_+ \rightarrow \mathbf{u}_m \rightarrow \mathbf{u}_0$ is not a global minimum because the MAP does not follow the dynamics once \mathbf{u}_m is reached. Obviously, the path $\mathbf{u}_+ \rightarrow \mathbf{u}_m \rightarrow \mathbf{u}_s \rightarrow \mathbf{u}_0$ theoretically has a smaller action than $\mathbf{u}_{+ \rightarrow 0}(t)$. From \mathbf{u}_m , the MAP $\mathbf{u}_{+ \rightarrow 0}(t)$ goes directly into the basin of attraction of \mathbf{u}_0 , along which the energy decays very fast. Due to the existence of the local residual, we need to clarify whether the choice made by the optimization solver is reasonable.

We compare the trajectories $U_{\mathbf{u}_{+ \rightarrow 0}(T_R)}(\tau)$ and $U_{\mathbf{u}_{+ \rightarrow 0}(28)}(\tau)$, where $\tau = 28$ is slightly larger than $T_R \approx 27$. It is seen that although the two initial states are very close to each other with an energy difference 1.1%, the difference in time needed for the energy to decay to the same level increases significantly. For instance, compared to $U_{\mathbf{u}_{+ \rightarrow 0}(28)}(\tau)$ the trajectory $U_{\mathbf{u}_{+ \rightarrow 0}(T_R)}(\tau)$ requires about 5000 more time units to decay to a state of energy 0.02. Then in the basin of attraction of \mathbf{u}_0 , the optimization solver has two choices to minimize the action functional: (1) try to follow the stable manifold of \mathbf{u}_s , which requires a long integration time and has a slow energy decay; (2) sacrifice a little action to go to a state, which yields a trajectory with a much faster energy decay. The second choice is chosen by the optimization solver due to the sensitivity of dynamics to the initial conditions around \mathbf{u}_m and the accumulation of the local residuals along a long numerical trajectory.

We now look into the MAP within the basin of attraction of \mathbf{u}_+ . It is seen that the energy of all trajectories $U_{\mathbf{u}_{+ \rightarrow 0}(t)}(\tau)$ with $t \leq T_L$ has a sharp decay at the beginning. A little shift along the ‘tangent’ direction of the energy curve can reach a state starting from which the energy of the trajectory decays even further. Since trajectories correspond to a zero action and the aforementioned shift is only of small deviation from the trajectories locally, it is reasonable that only a small action is needed to achieve such a shift. Although such a mechanism gives rise to incorrect MAP within the basin of \mathbf{u}_0 , it is actually preferred with the basin of attraction of \mathbf{u}_+ since it can bring the MAP to the stable manifold of \mathbf{u}_s at a small cost of action. Apparently, the scenario is similar with that for the MAP $\mathbf{u}_{0 \rightarrow s}$. The difference is that $\mathbf{u}_{0 \rightarrow s}$ looks for states with initial energy growth while $\mathbf{u}_{+ \rightarrow 0}$ looks for states with initial energy decay. Both MAPs

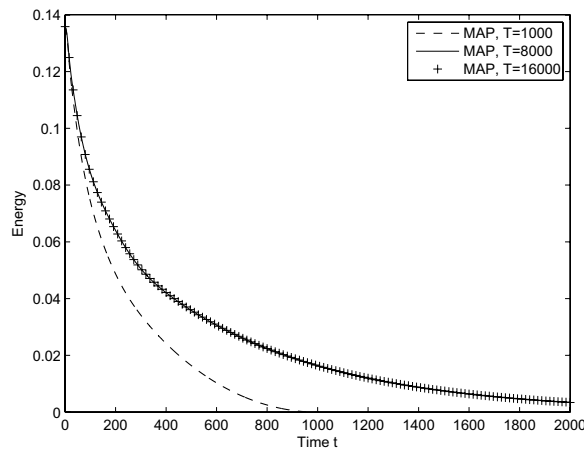


Figure 10. Energy evolution along MAPs $\mathbf{u}_{+\rightarrow 0}(t)$ given by integration time $T = 10^3, 8 \times 10^3, 1.6 \times 10^4$.

Table 1. Some results about \mathbf{u}_m for $Re = 3150$. We consider the MAPs that start from the same starting point as MAP $\mathbf{u}_{+\rightarrow 0}$, and end at different locations. Let $\mathbf{u}_m^- = \mathbf{u}_{+\rightarrow 0}(T_L)$ and $\mathbf{u}_m^+ = \mathbf{u}_{+\rightarrow 0}(T_R)$. $|T_R - T_L| = 10^{-4}$.

| | \mathbf{u}_m^+ | $U_{\mathbf{u}_m^+}(1)$ | $U_{\mathbf{u}_m^+}(2)$ | $U_{\mathbf{u}_m^-}(1)$ | $U_{\mathbf{u}_m^-}(2)$ |
|---------------------|------------------|-------------------------|-------------------------|-------------------------|-------------------------|
| Action | 9.7218e-6 | 9.7010e-6 | 9.7148e-6 | 9.7010e-6 | 9.7148e-6 |
| Action(de-aliasing) | 9.8586e-6 | 9.8371e-6 | 9.8509e-6 | 9.8371e-6 | 9.8509e-6 |

try to save action using the fact that a trajectory needs zero action, which is possible due to the properties of the O–S operator.

5.3.2. Discussion of \mathbf{u}_m . We now examine the relation between \mathbf{u}_m and the integration time T . In figure 10 we plot the energy along the MAPs given by integration time $T = 1 \times 10^3, 8 \times 10^3, 1.6 \times 10^4$. It seen that the MAPs given by $T = 8 \times 10^3, 1.6 \times 10^4$ are almost the same, while the MAP given by $T = 10^3$ has a faster energy decay due to the smaller integration time, which affects the location of \mathbf{u}_m on the stable manifold of \mathbf{u}_s . The transition time T_s 's are 25.5751, 26.9968 and 26.9689, respectively, for the MAPs $\mathbf{u}_{+\rightarrow 0}$ with $T = 10^3, 8 \times 10^3, 1.6 \times 10^4$, and the corresponding actions from \mathbf{u}_+ to \mathbf{u}_m are $1.007 \times 10^{-5}, 9.718 \times 10^{-6}$ and 9.717×10^{-6} . In other words, if we increase the integration time, the MAM will yield the same \mathbf{u}_m .

Since the MAP $\mathbf{u}_{+\rightarrow 0}$ is not correct within the basin of attraction of \mathbf{u}_0 , we need to zoom in the behaviour of the MAP in the neighbourhood of \mathbf{u}_m . The main question is: Can \mathbf{u}_m be reached?

To address this question, we look for the MAPs that have the same starting point as $\mathbf{u}_{+\rightarrow 0}(t)$ but end at $\mathbf{u}_m^+, U_{\mathbf{u}_m^+}(1), U_{\mathbf{u}_m^+}(2), U_{\mathbf{u}_m^-}(1)$ and $U_{\mathbf{u}_m^-}(2)$, respectively, using tMAM [46], where $\mathbf{u}_m^+ = \mathbf{u}_{+\rightarrow 0}(T_R), \mathbf{u}_m^- = \mathbf{u}_{+\rightarrow 0}(T_L)$ and $|T_R - T_L| = 10^{-4}$. The reason that we only run the dynamic solver for a short time is to reduce the effect of local residuals. The corresponding actions given by these MAPs are summarized in table 1, where the actions with de-aliasing are computed with doubled Gauss-type quadrature points in each direction, i.e., t -, x -, and y -direction, see appendix C.1 for the discussion about aliasing errors.

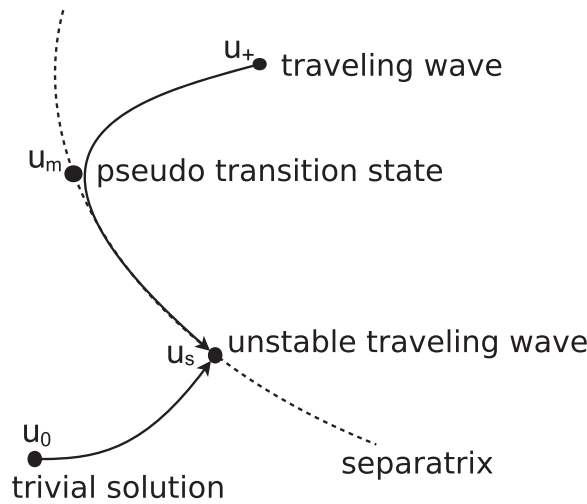


Figure 11. A diagram for the transition mechanism between \mathbf{u}_0 (trivial solution) and \mathbf{u}_+ (travelling wave). The unstable travelling wave is \mathbf{u}_s and the pseudo transition state is \mathbf{u}_m .

First of all, the action from \mathbf{u}_+ to \mathbf{u}_m^+ given by tMAM is 9.7218×10^{-6} corresponding to an optimal integration time 26.9679, in contrast to the action 9.7221×10^{-6} and the time $T_R = 26.9688$, respectively, given by $\mathbf{u}_{+\rightarrow 0}(t)$. Thus, the time resolution of $\mathbf{u}_{+\rightarrow 0}$ is good enough although a large T is used for aMAM to compute $\mathbf{u}_{+\rightarrow 0}$. Second, for a small integration time, we are able to afford the computation cost for de-aliasing. It is seen that the aliasing error does affect the action. The relative error is about 1%, which is acceptable. Third, \mathbf{u}_m cannot be reached. It is seen that $|T_R - T_L|$ is small enough such that the actions from \mathbf{u}_+ to $U_{\mathbf{u}_m^+}(\tau)$ and $U_{\mathbf{u}_m^-}(\tau)$ are the same for $\tau \leq 2$. So we can regard that $U_{\mathbf{u}_m^+}(\tau)$ is located on the separatrix. We see that the action from \mathbf{u}_+ to $U_{\mathbf{u}_m^+}(1)$, which is 9.7010×10^{-6} , is actually smaller than the action from \mathbf{u}_+ to \mathbf{u}_m^+ , which is 9.7218×10^{-6} . Thus the mechanism implied by figure 9 is still valid here. More specifically, within the basin of attraction of \mathbf{u}_+ , the MAP should first approach \mathbf{u}_m and bend at a location $\tilde{\mathbf{u}}_m$ close to \mathbf{u}_m such that a smaller action can be reached by making a little local shift along the “tangent” direction of the energy curve to get closer to the separatrix. Since the actions from \mathbf{u}_+ to \mathbf{u}_m^+ and $U_{\mathbf{u}_m^+}(1)$ are very close, the location $\tilde{\mathbf{u}}_m$ should be close to \mathbf{u}_m . From $\tilde{\mathbf{u}}_m$, the MAP should try to follow the dynamics on one hand, and sacrifice a little action to get closer to the separatrix on the other hand. Such a process should end at the unstable travelling wave \mathbf{u}_s . We also note that the action from \mathbf{u}_+ to $U_{\mathbf{u}_m^+}(2)$ is slightly larger than the action from \mathbf{u}_+ to $U_{\mathbf{u}_m^+}(1)$, which is reasonable due to the accumulation of the local residuals. Fourth, the turning point $\tilde{\mathbf{u}}_m$ is very close to the separatrix, which implies the action from $\tilde{\mathbf{u}}_m$ to \mathbf{u}_s is very close to zero. In other words, The following two paths

$$I : \mathbf{u}_+ \rightarrow \tilde{\mathbf{u}}_m \rightarrow \mathbf{u}_s \rightarrow \mathbf{u}_0 \quad \text{and} \quad II : \mathbf{u}_+ \rightarrow \mathbf{u}_m \rightarrow \mathbf{u}_s \rightarrow \mathbf{u}_0 \quad (21)$$

have almost the same action. Before \mathbf{u}_s is reached, path I is completely located within the domain of attraction of \mathbf{u}_+ while part of path II is located on the separatrix. The MAP should be consistent with path I, which means that \mathbf{u}_s is the transition state. However, since $\tilde{\mathbf{u}}_m$ is very close to \mathbf{u}_m , we regard \mathbf{u}_m as a pseudo transition state (see figure 11) due to its distinctiveness.

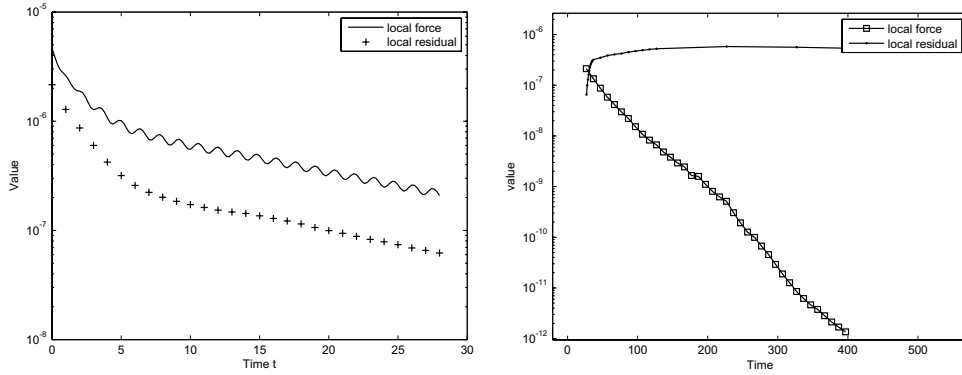


Figure 12. Left: local force $\|F_{\mathbf{u}_{+\rightarrow 0}}(t, \mathbf{x})\|_2^2$ and local residual $\|R_{\mathbf{u}_{+\rightarrow 0}(t)}(0^+, \mathbf{x})\|_2^2$ along the MAP $\mathbf{u}_{+\rightarrow 0}$. Right: local force $\|F_{\mathbf{u}_{+\rightarrow 0}}(t, \mathbf{x})\|_2^2$ along the MAP $\mathbf{u}_{+\rightarrow 0}(t)$ for $t \geq T_s$ and local residual $\|R_{\mathbf{u}_{+\rightarrow 0}(T_s)}(\tau, \mathbf{x})\|_2^2$. The horizontal axis is shared by t and τ . For the local force, the horizontal axis indicates time t ; for the local residual, the horizontal axis indicates $T_s + \tau$.

5.3.3. The MAP from the vicinity of \mathbf{u}_m to \mathbf{u}_s . We now try to clarify why the MAP $\mathbf{u}_{+\rightarrow 0}$ does not follow the separatrix. From the discussions in the previous section, we see that the MAP from $\tilde{\mathbf{u}}_m$ to \mathbf{u}_s should be located within a very thin boundary layer against the separatrix. Thus the action from $\tilde{\mathbf{u}}_m$ to \mathbf{u}_s is almost zero. Roughly speaking, the nonzero numerical action given by a trajectory from \mathbf{u}_m to \mathbf{u}_s can be regarded as the error induced by the numerical approximation. We here mainly check the local residual $R_{\mathbf{u}_{+\rightarrow 0}(t)}(\tau, \mathbf{x})$ and local force $F_{\mathbf{u}_{+\rightarrow 0}}(t, \mathbf{x})$.

There are several observations that we should keep in mind: (1) from \mathbf{u}_m to \mathbf{u}_s the dynamics solver will take $O(10^3)$ time units, see figure 9; (2) the energy decay along the trajectory from \mathbf{u}_m to \mathbf{u}_s is very slow in contrast to the fast energy decay along the MAP starting from \mathbf{u}_m . (3) When a trajectory converges to \mathbf{u}_0 , the high order modes will first damp.

In the left plot of figure 12, we compare the force $\|F_{\mathbf{u}_{+\rightarrow 0}}(t, \mathbf{x})\|_2^2$ and the residual $\|R_{\mathbf{u}_{+\rightarrow 0}(t)}(0^+, \mathbf{x})\|_2^2$ for $t \leq T_s$. It is seen that within the domain of attraction of \mathbf{u}_+ , the force is always larger than the residual of a trajectory starting from the same point on the MAP, which is what we expected.

In the right plot of figure 12, we plot the force $\|F_{\mathbf{u}_{+\rightarrow 0}}(t, \mathbf{x})\|_2^2$ along the MAP $\mathbf{u}_{+\rightarrow 0}$ for $t \geq T_s$ and the residual $\|R_{\mathbf{u}_{+\rightarrow 0}(T_s)}(\tau, \mathbf{x})\|_2^2$ with respect to τ for the trajectory $U_{\mathbf{u}_{+\rightarrow 0}(T_s)}(\tau)$. It is seen that although initially $\|R_{\mathbf{u}_{+\rightarrow 0}(T_s)}(0^+, \mathbf{x})\|_2^2$ is smaller than $\|F_{\mathbf{u}_{+\rightarrow 0}}(T_s, \mathbf{x})\|_2^2$, the dynamic solver will overall maintain a large residual of $O(10^{-7})$ for a time of $O(10^3)$ from \mathbf{u}_m to \mathbf{u}_s . The large residual reflects that on the separatrix the high-order modes are relatively strong which introduce more numerical errors due to the nonlinearity of N-S operator. If the MAP follows the trajectory $U_{\mathbf{u}_{+\rightarrow 0}(T_s)}(\tau)$, it will have an action of $O(10^{-4})$, which is basically the accumulated local residuals. Instead, the MAP follows a different path within the basin of attraction of \mathbf{u}_0 , along which the high-order modes decay much more quickly such that errors induced by high-order modes can be reduced. When the high-order modes are weak enough, the MAP actually becomes a trajectory to \mathbf{u}_0 . It can be seen in figure 9 the energy decay of the trajectory starting from \mathbf{u}_s is very similar with the MAP starting from a state of the same energy level.

Recall that a similar issue occurs for the MAP $\mathbf{u}_{0 \rightarrow +}$. Although both $\mathbf{u}_{0 \rightarrow +}$ and $\mathbf{u}_{+\rightarrow 0}$ are affected by the local residuals induced by spatial discretization, there is a fundamental difference between them. For the trajectory $U_{\mathbf{u}_s}(\tau)$, the local residual $\|R_{\mathbf{u}_s}(\tau, \mathbf{x})\|_2^2$ oscillates

Table 2. Energy of \mathbf{u}_s , \mathbf{u}_m , \mathbf{u}_+ and actions required for transitions between \mathbf{u}_0 and \mathbf{u}_+ .

| Re | $E_V(\mathbf{u}_s)$ | $E_V(\mathbf{u}_m)$ | $E_V(\mathbf{u}_+)$ | $S_{T_s}(\mathbf{u}_0 \rightarrow +)$ | $S_{T_s}(\mathbf{u}_+ \rightarrow 0)$ | $r_{0 \leftrightarrow +}$ |
|------|---------------------|---------------------|---------------------|---------------------------------------|---------------------------------------|---------------------------|
| 3100 | 7.34e-2 | 1.08e-1 | 1.18e-1 | 3.22e-5 | 6.58e-6 | 4.89 |
| 3120 | 4.77e-2 | 1.11e-1 | 1.25e-1 | 1.98e-5 | 7.96e-6 | 2.49 |
| 3130 | 3.60e-2 | 1.13e-1 | 1.29e-1 | 1.40e-5 | 8.55e-6 | 1.76 |
| 3140 | 3.50e-2 | 1.15e-1 | 1.32e-1 | 1.35e-5 | 9.07e-6 | 1.49 |
| 3150 | 3.41e-2 | 1.17e-1 | 1.36e-1 | 1.31e-5 | 9.72e-6 | 1.35 |
| 3190 | 3.12e-2 | 1.23e-1 | 1.49e-1 | 1.17e-5 | 1.18e-5 | 0.99 |
| 3200 | 3.07e-2 | 1.25e-1 | 1.52e-1 | 1.14e-5 | 1.22e-5 | 0.93 |
| 3250 | 2.74e-2 | 1.33e-1 | 1.67e-1 | 9.90e-6 | 1.46e-5 | 0.68 |
| 3330 | 2.34e-2 | 1.45e-1 | 1.89e-1 | 8.34e-6 | 1.79e-5 | 0.47 |
| 3410 | 2.14e-2 | 1.57e-1 | 2.10e-1 | 7.26e-6 | 2.08e-5 | 0.35 |
| 3500 | 1.88e-2 | 1.70e-1 | 2.33e-1 | 6.15e-6 | 2.39e-5 | 0.26 |

around a certain level within the domain of attraction of \mathbf{u}_+ because high-order modes are important there, and their accumulation can be dominant due to the long relaxation time and completely misleads the optimization solver to a wrong transition state. Then we need to adjust the final state of the MAP to get rid of the part from \mathbf{u}_s to \mathbf{u}_+ , i.e., we only consider the MAP $\mathbf{u}_0 \rightarrow s$. For the MAP $\mathbf{u}_+ \rightarrow 0$, the quick escape from the basin of attraction of \mathbf{u}_+ is actually in favour of the transition and the fast energy damping of high-order modes in the domain of attraction of \mathbf{u}_0 makes the local residuals also decay quickly to zero. We then think that the action from \mathbf{u}_+ to \mathbf{u}_m can be regarded as a reasonable approximation of the action from \mathbf{u}_+ to \mathbf{u}_0 especially when Re is relatively large. For example, when $Re = 3100$, $S_{T_s}(\mathbf{u}_+ \rightarrow 0)$, the action from \mathbf{u}_+ to \mathbf{u}_m , is 6.58×10^{-6} , and $S_T(\mathbf{u}_+ \rightarrow 0) - S_{T_s}(\mathbf{u}_+ \rightarrow 0)$, the action from \mathbf{u}_m to \mathbf{u}_0 , is 3.75×10^{-6} . When $Re = 3200$, $S_{T_s}(\mathbf{u}_+ \rightarrow 0) = 1.22 \times 10^{-5}$ and $S_T(\mathbf{u}_+ \rightarrow 0) - S_{T_s}(\mathbf{u}_+ \rightarrow 0) = 2.27 \times 10^{-6}$. In other words, the action within the domain of action of \mathbf{u}_+ will soon become dominant for $Re > Re_G$. Our main concern about the action $S_T - S_{T_s}$ is that it might affect the exit location if it is too large. Since the action S_{T_s} is dominant for $\mathbf{u}_+ \rightarrow 0$, we do not expect that \mathbf{u}_m deviates dramatically.

5.4. A summary about the transition mechanism between \mathbf{u}_0 and \mathbf{u}_+

To this end, we can summarize our understanding of the transition mechanism between \mathbf{u}_0 and \mathbf{u}_+ . For the transition from \mathbf{u}_0 to \mathbf{u}_+ , the MAP will escape the basin of attraction of \mathbf{u}_0 through the unstable travelling wave \mathbf{u}_s ; for the transition from \mathbf{u}_+ to \mathbf{u}_0 , the MAP should take path I given in (21), where we can regard \mathbf{u}_m located on the separatrix as a pseudo transition state. Such a transition mechanism is illustrated in figure 11.

5.5. Critical Reynolds number based on the action

We now consider the transition between \mathbf{u}_0 and \mathbf{u}_+ for some Reynolds numbers $Re \in (Re_G, Re_L)$, where the action $S_{T_s}(\mathbf{u}_0 \rightarrow +)$ and $S_{T_s}(\mathbf{u}_+ \rightarrow 0)$ required for transition are computed using the strategies described in sections 5.2 and 5.3, and we approximate the ratio $r_{0 \leftrightarrow +}$ as

$$r_{0 \leftrightarrow +} = \frac{V(\mathbf{u}_0, \mathbf{u}_+)}{V(\mathbf{u}_+, \mathbf{u}_0)} \approx \frac{S_{T_s}(\mathbf{u}_0 \rightarrow s)}{S_{T_s}(\mathbf{u}_+ \rightarrow 0)}. \tag{22}$$

All computations are based on the integration time $T = 8 \times 10^3$. The aMAM is employed. $N_e = 3072$ finite elements are used in time direction, where fifth-order polynomials are used in each element. The results are summarized in table 2.

We have several interesting observations from table 2. First, the critical states for the nonlinear instability of \mathbf{u}_0 and \mathbf{u}_+ are different. The unstable travelling wave \mathbf{u}_s is more important for the stability of \mathbf{u}_0 while the pseudo transition state \mathbf{u}_m is more important for the stability of \mathbf{u}_+ , because the action from \mathbf{u}_0 to \mathbf{u}_s is comparable to that from \mathbf{u}_+ to \mathbf{u}_m . Second, it is seen that as the Reynolds number increases, the action needed to escape the basin of attraction of \mathbf{u}_0 decreases while the action needed to escape the basin of attraction of \mathbf{u}_+ increases. Due to the existence of \mathbf{u}_m , the transition from \mathbf{u}_+ to \mathbf{u}_0 is not difficult to achieve although the trajectory starting from \mathbf{u}_m needs to travel a long time along the separatrix to \mathbf{u}_s before it quickly decays to \mathbf{u}_0 . Simply speaking, as Reynolds number increases, \mathbf{u}_s moves closer to \mathbf{u}_0 , indicating by its decreasing energy, and \mathbf{u}_+ always stays close to the stable manifold of \mathbf{u}_s , indicating by a small action from \mathbf{u}_+ to \mathbf{u}_m . Third, it seems reasonable to define a probabilistic critical number Re_A discussed in section 3. The ratio $r_{0 \leftrightarrow +}$ drops fast with respect to Reynolds number and $r_{0 \leftrightarrow +} \approx 1$ around $Re_A \approx 3190$ indicating the comparable metastability of \mathbf{u}_0 and \mathbf{u}_+ in the asymptotic sense.

Although the transition behaviour between \mathbf{u}_0 and \mathbf{u}_+ appears qualitatively reasonable, we do not expect $Re_A \approx 3190$ is a sharp estimate, since only four harmonics have been employed in x direction. We have seen that the local residuals introduce many troubles in our numerical experiments because there is not enough information about high-order modes to deal with the nonlinearity of N–S operator within the domain of attraction of \mathbf{u}_+ . We then increase the number of harmonics in x direction from 4 to 15, and the number of Legendre modes in y direction from 32 to 48. Due to the expensive computation cost, we only checked the Reynolds number 3500 for the fine resolution.

First of all, the transition mechanism given by the fine resolution is qualitatively consistent with that given by the coarse resolution. We plotted the energy evolution of the MAP $\mathbf{u}_{+ \rightarrow 0}$ and trajectories $U_{\mathbf{u}_{+ \rightarrow 0}(t)}(\tau)$ for different t in figure 13. It is seen that figure 13 is consistent with figure 9. Second, the corresponding actions needed for transition are quantitatively different. The action from \mathbf{u}_0 to \mathbf{u}_+ given by the fine resolution is 4.69×10^{-6} in contrast to the corresponding action 6.15×10^{-6} given by the coarse resolution. The action from \mathbf{u}_+ to \mathbf{u}_0 given by the fine resolution is 3.34×10^{-6} in contrast to the corresponding action 2.39×10^{-5} given by the coarse resolution. Both actions become smaller for the fine resolution since the approximation of the phase space becomes better. In particular, the action for the transition from \mathbf{u}_+ to \mathbf{u}_0 decays significantly from the coarse resolution to the fine resolution, which is almost one order in magnitude although the energy of \mathbf{u}_m given by the fine resolution is 0.164, close to the one 0.170 given by the coarse resolution, see table 2. The reason of such a big change is twofold: (1) the coarse resolution does a good job in the domain of attraction of \mathbf{u}_0 because low-order modes are more important there; (2) the high-order modes are more important within the domain of attraction of \mathbf{u}_+ , but the coarse resolution is not able to provide enough information about the high-order modes.

Since the coarse resolution provides the subcritical bifurcation, we can always consider transitions in the corresponding phase space. Thus, Re_A given by table 2 only makes sense for the coarse phase space. To study Re_A for the N–S equations, we need a finer phase space. We also note that Re_A should also depend on the channel length L . At this moment, we do not have a good approximation of Re_A in terms of both Re and L . However, the current understanding about the transitions in a coarse phase space is helpful for us to investigate this issue.

Remark 4. One drawback of the current definition of Re_A is that it depends on the modelling of the random force. In this work, we consider the space-time white noise, which is the most ideal case from the mathematical point of view. If we can obtain a better mathematical model of the noise, the action functional S_T should change accordingly, which yields the corresponding

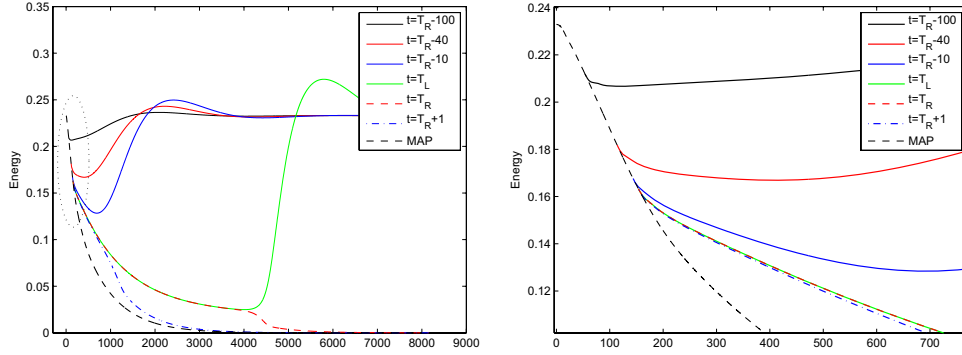


Figure 13. Left: energy evolution of MAP $\mathbf{u}_{+\rightarrow 0}$ and trajectories $U_{\mathbf{u}_{+\rightarrow 0}(t)}(\tau)$, where the MAP $\mathbf{u}_{+\rightarrow 0}$ is computed with $T = 8 \times 10^3$. t and τ share the horizontal axis. For the MAP, the horizontal axis indicates t ; for the trajectories $U_{\mathbf{u}_{+\rightarrow 0}(t)}(\tau)$, the horizontal axis indicate $t + \tau$ with a fixed t . $Re = 3500$. The spatial resolution is given by 15 harmonics in the x direction and 48 Legendre modes in the y direction. Right: close-up view of the region marked by the eclipse in the left plot.

critical Reynolds number Re_A , see remark 7 in the appendix. However, we think that the current model of noise should capture the main properties of the critical Reynolds number Re_A , which can be used as a reference for further study of specific noise.

Remark 5. A recent study on the laminar-turbulent boundary of 3D plane Couette flow in [25] shows that the stable manifold of the saddle state may wrap around a chaotic saddle, and thus a transition from turbulence to laminar flow may first jump onto the chaotic saddle and then approach the saddle state along its stable manifolds before finally converges to the steady state, i.e., the laminar flow. For our problem the structure of the separatrix is very simple. However, the role of \mathbf{u}_m is to some extent similar to the role of the aforementioned chaotic saddle in the sense that it is a state that is relatively easy to reach from the non-trivial attractor before a trajectory to \mathbf{u}_0 can be found.

5.6. Development of the nonlinear instability of \mathbf{u}_0 and \mathbf{u}_+

Since the transition mechanisms given by the coarse spatial resolution and the fine one are qualitatively consistent, we here focus on transitions at $Re = 3500$ given by the fine spatial resolution. In figure 14, we plot the energy evolution of $U_{\mathbf{u}_0 \rightarrow s}(T_L)(\tau)$ and $U_{\mathbf{u}_0 \rightarrow s}(T_R)(\tau)$. The close-up view suggests that the MAP actually first lands onto the stable manifold of the unstable solution $\mathbf{u}_s(t)$ at a state, which has a slightly smaller energy than $\mathbf{u}_s(t)$. This is possible due to the nonmodal stability theory. In figure 15, we plot a number of snapshots of vorticity with streamlines at a certain moment of the MAPs $\mathbf{u}_0 \rightarrow s(t)$ and $\mathbf{u}_+ \rightarrow 0(t)$ with $t < T_s$.

For the MAP $\mathbf{u}_0 \rightarrow s(t)$, we plot the snapshots at time $t = 0.85T_s, 0.90T_s, 0.93T_s, 0.96T_s$, and T_s . For the time $t \lesssim 0.85T_s$, the velocity field mainly corresponds to a shear flow, where the horizontal velocity is dominant, also see figure 6. As the vertical velocity becomes stronger, two vortices start to emerge, one is from the top wall and the other one is from the bottom wall. As the size of the vortices increases, the flow becomes more oscillating although the energy is relatively small. As soon as the state \mathbf{u}_s is reached, which has an energy about 0.018, no action will be required for the transition to \mathbf{u}_+ .

For the MAP $\mathbf{u}_+ \rightarrow 0(t)$, we plot the snapshots at time $t = 0, 0.25T_s, 0.5T_s, 0.75T_s$ and T_s . The energy of the travelling wave is about 0.233. Starting from the travelling wave, the

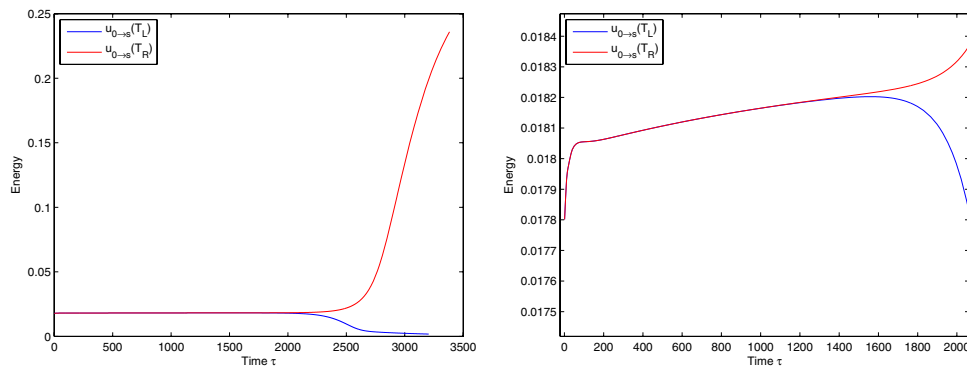


Figure 14. Energy evolution of the dynamic solver starting from $\mathbf{u}_{0 \rightarrow s}(T_L)$ and $\mathbf{u}_{0 \rightarrow s}(T_R)$. The right plot is a close-up view of the left one.

main observation is that the flow becomes less and less oscillating before the transition time T_s . Although the energy keeps decreasing, the energy of the pseudo transition state \mathbf{u}_m is relatively large, which is about 0.164, in contrast to the energy 0.018 of the transition state \mathbf{u}_s . In other words, there is a large energy gap between \mathbf{u}_m and \mathbf{u}_s , where no action is needed from \mathbf{u}_m to \mathbf{u}_s .

Based on the above observations, we pay attention to two issues for the transitions between \mathbf{u}_0 and \mathbf{u}_+ : energy and spatial pattern. First, the transition state \mathbf{u}_s has a relatively small energy but a very oscillating spatial pattern, which implies that as long as enough energy is provided to form the oscillating pattern, the oscillation can be self-sustained and eventually evolves to \mathbf{u}_+ . Second, for the transition from \mathbf{u}_+ to \mathbf{u}_0 , the most effective way to use the action appears to change the spatial pattern, where a very large decay of energy is not quite necessary. Once the spatial pattern of the pseudo transition state \mathbf{u}_m is formed, the oscillation cannot be self-sustained any more and eventually decays to zero.

The spatial pattern is nothing but the distribution of energy at each mode of the approximation space. In figure 16, we plot the energy contribution of Fourier modes with respect to the wave number for the vertical velocity at the centre line $y = 0$. Only odd modes are plotted due to the much smaller contribution from the even modes. First, according to approximation theory, the spectral method converges exponentially fast to approximate a smooth function, which implies that the energy contribution decays exponentially with respect to the wave number. It is seen in figure 16 that the exponential convergence holds up to a certain accuracy for \mathbf{u}_s , \mathbf{u}_m and \mathbf{u}_+ . Second, compared to \mathbf{u}_+ , the energy of each Fourier mode of \mathbf{u}_s and \mathbf{u}_m drops, but the energy of high-order modes drops much faster than that of slower modes.

6. Summary and discussions

In this paper, we established a connection between the nonlinear stability of wall-bounded shear flows and the small random perturbations of N–S equations through the F–W theory of large deviations. Due to the existence of noise, the coexisting stable solutions of deterministic N–S equations become metastable. When the noise is small enough, the metastability can be characterized in the asymptotic sense by the minimal action path or the quasi-potential. Such a metastability also provides a possibility to define a critical Reynolds number, at which the transition probabilities between the base flow and the other sustainable state are asymptotically equal to each other. We applied this action-based stability theory to the 2D Poiseuille flow in

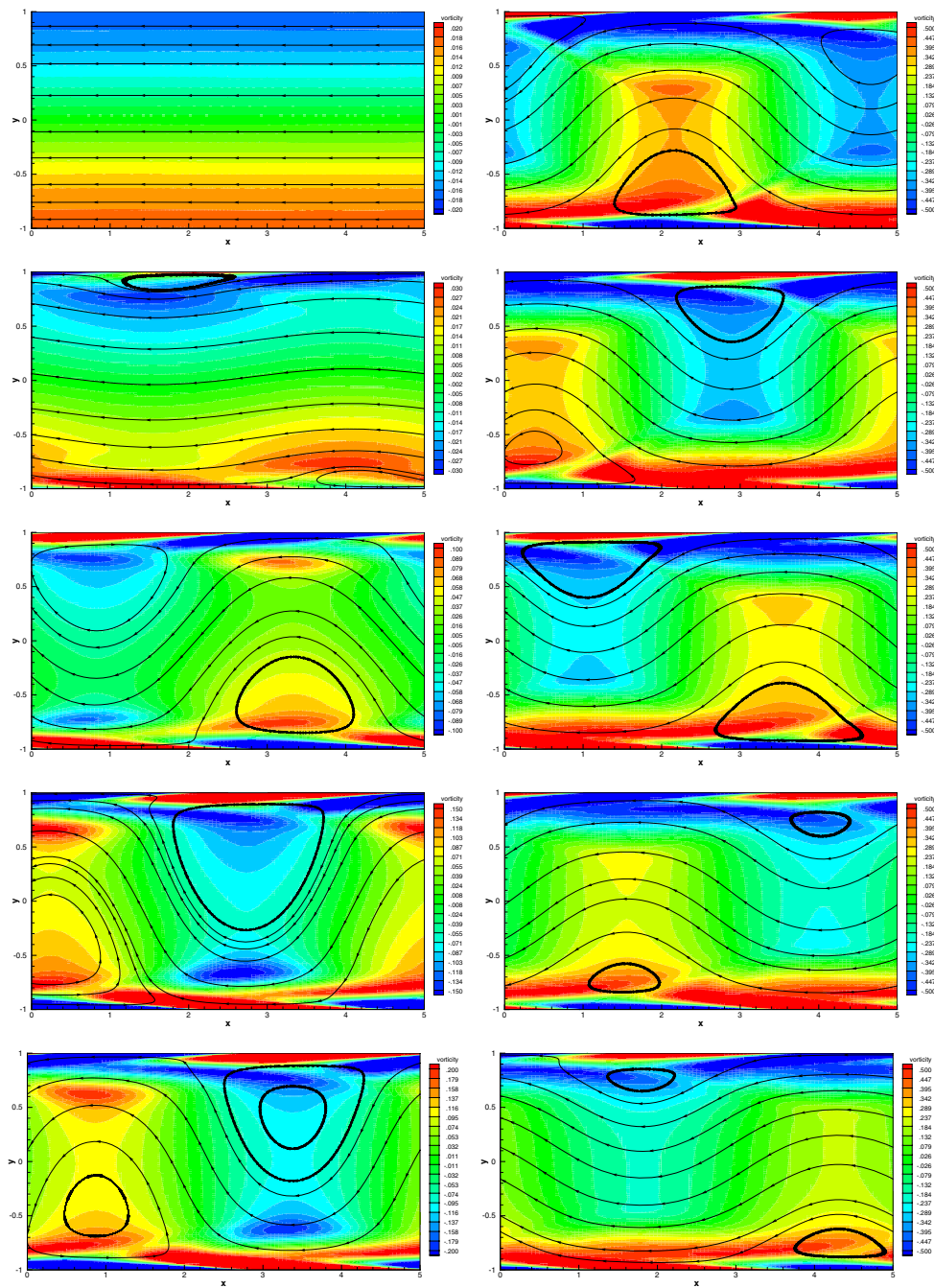


Figure 15. Snapshots of vorticity with streamlines on the MAPs $\mathbf{u}_{0 \rightarrow s}$ and $\mathbf{u}_{+ \rightarrow 0}$. The results given by the fine spatial resolution with 15 harmonics in the x direction and 48 Legendre modes in the y direction at $Re = 3500$. The left column consists of snapshots for the MAP $\mathbf{u}_{0 \rightarrow s}$ at $t = 0.85T_s, 0.90T_s, 0.93T_s, 0.96T_s, T_s$ from top to bottom. The right column consists of snapshots for the MAP $\mathbf{u}_{+ \rightarrow 0}$ at $t = 0, 0.25T_s, 0.50T_s, 0.75T_s, T_s$.

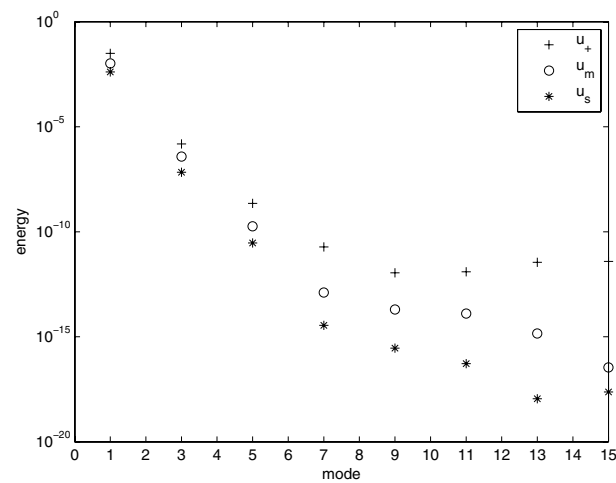


Figure 16. Energy contribution of Fourier modes of vertical velocity at the centre line $y = 0$ with respect to the wave number. Only the odd wave numbers are plotted since the contribution from the even wave numbers are very small.

a short channel, where the upper-branch stable solution takes the form of a travelling wave. The following observations are of particular interest:

- The unstable travelling wave plays an important role for the instability of the base flow while for the stability of the travelling wave, the pseudo transition state on the separatrix is more critical than the unstable travelling wave. This is mainly due to the fact that N–S equations correspond to a non-gradient system.
- It is the interaction between energy and spatial pattern that affects how to escape the basin of attraction of either the base flow or the travelling wave. The transition state from the base flow to the travelling wave is of low energy and high oscillation; the pseudo transition state from the travelling wave to the base flow is of high energy and of low oscillation.
- There exists a large gap between the unstable travelling wave and the pseudo transition state for the transition from the travelling wave to the base flow. The existence of dynamics from the pseudo transition state to the unstable travelling wave can make the transitions between the base flow and the travelling wave complicated.

Many issues have been identified from both numerical and physical points of view through studying the subcritical bifurcation given by the 2D Poiseuille flow in a short channel. From the numerical point of view, the following issues deserve more attention:

- Considering the interaction between the local force and the local residual, the dynamic solver and MAM should be addressed in a more unified framework.
- The computation cost is still a severe barrier for the application of LDP, where algorithm improvement is still needed. Possible numerical issues include: (1) a more effective optimization procedure. The main difficulty is to deal with the divergence-free constraint, i.e., the pressure. (2) Adaptivity in time direction. For instance, from the discussions in section 5.6, we see that the main transition from \mathbf{u}_0 to \mathbf{u}_s occurs after $0.85T_s$, which corresponds to a fast energy growth in a relative short period of time. Such a physical phenomenon should be integrated better into numerical algorithms. (3) A more effective preconditioner. This issue is particularly important for 3D cases.

From the physical point of view, the most interesting question is whether 3D cases can be studied using the same methodology. Such a generalization is straightforward although some mathematical issues related noise deserve more attention. However, a direct application of MAM to 3D cases is still difficult. The reason is twofold: (1) the minimum action method for Navier–Stokes equations needs more understanding from the numerical point of view, and (2) the computation cost given by the current version of MAM is still too high for 3D cases.

Appendix A. Small random perturbations in initial conditions

In this work, we mainly focus on the nonlinear instability from the transition point of view, where the small noise is located in the force. We can also employ the LDP to consider small random perturbations in initial conditions

$$\mathbf{u}(t = 0, \mathbf{x}) = \mathbf{u}_0 + \sqrt{\varepsilon}G(\mathbf{x}), \tag{A.1}$$

where $G(\mathbf{x})$ is a Gaussian field in a divergence-free space subject to a covariance operator K . For this case, the Navier–Stokes (N–S) equations remain deterministic. The rate functional for the scaled Gaussian field is defined as [39]

$$S(\tilde{\mathbf{u}}(\mathbf{x})) = \frac{1}{2} \|K^{-\frac{1}{2}}\tilde{\mathbf{u}}\|_2^2, \tag{A.2}$$

where the L_2 norm is taken on the physical domain D . If N–S equations depend continuously on the initial conditions, we can use the contraction principle [39] to define the following optimization problem

$$S(\tilde{\mathbf{u}}^*) = \min_{\substack{\mathbf{u}(0)=\mathbf{u}_0+\tilde{\mathbf{u}}(\mathbf{x}) \\ \mathbf{u}(\infty)=\mathbf{u}_+}} S(\tilde{\mathbf{u}}), \tag{A.3}$$

where \mathbf{u} is the solution of the deterministic N–S equations and $\tilde{\mathbf{u}}$ is a perturbation that triggers the instability of \mathbf{u}_0 . Then the LDP says that

$$\Pr(\text{Initial random perturbations trigger the instability of } \mathbf{u}_0) \asymp e^{-\frac{S(\tilde{\mathbf{u}}^*)}{\varepsilon}}, \tag{A.4}$$

which implies that the occurrence of the instability of \mathbf{u}_0 is mainly determined by one deterministic perturbation profile $\tilde{\mathbf{u}}^*(\mathbf{x})$. The reason that $\tilde{\mathbf{u}}^*(\mathbf{x})$ is important is twofold. First, among all perturbations that can trigger the instability of \mathbf{u}_0 , $\tilde{\mathbf{u}}^*(\mathbf{x})$ is the most probable one, which has the smallest weighted L_2 norm. Second, since it has been realized that the spatial pattern of perturbations is one important factor for the instability of \mathbf{u}_0 , what information we can obtain from the spatial pattern of the most probable profile $\tilde{\mathbf{u}}^*(\mathbf{x})$ becomes an interesting problem.

Remark 6. The above strategy given by the LDP has a close relation to the idea of minimal seeds [36], which seeks the perturbation of the smallest kinetic energy that induces the fastest transient energy growth. First, the optimization problem (A.3) is overall a PDE constrained problem, which is similar to the optimization approach used for minimal seeds [36]. The difference is that the norm in equation (A.2) is defined by the LDP while for minimal seeds the corresponding norm is usually based on physical intuition. Second, it is seen from equation (A.3) that if K is an identity operator, the rate functional is nothing but the kinetic energy. The identity covariance operator corresponds that the perturbation is white noise. In general, we require that the covariance operator K is symmetric, positive definite and of trace class, i.e., its eigenvalues are real and positive, and their sum is finite. Although the identity operator in an infinite dimensional space is not of trace class, the approximated white noise is always finite dimensional and of trace class. From the LDP, we can regard that the

perturbation of the smallest kinetic energy is the most probable one that triggers the instability of the base flow when the perturbations are modelled by white noise. Third, if K is not an identity operator, i.e., the noise is coloured, we then need to minimize the weighted kinetic energy to find the most probable noise profile instead of the regular kinetic energy. This way, we are able to study the effect of correlation length of noise on the instability of \mathbf{u}_0 . Coupling the LDP and the idea of minimal seeds, we can ask the following question: what is the most probable perturbation profile that induces the fastest transient energy growth if the perturbation is given by a Gaussian field subject to a covariance operator K ?

Remark 7. Using the same strategy discussed in remark 6, we can relax the random force in equation (8) to Hilbert space valued Wiener process subject to a covariance operator K . In other words, we introduce correlation in space and the noise remains white in the time direction.

Appendix B. MAM with optimal linear time scaling for the N–S equations

First of all, we choose the same finite element approximation space given in equation (20) of [40]. We use action functional with respect to both \mathbf{u} and p , which takes a form

$$S_T(\mathbf{u}, p) = \frac{1}{2} \int_0^T \left\| \frac{\partial \mathbf{u}}{\partial t} - (\mathbf{u}_{\text{tot}} \cdot \nabla) \mathbf{u}_{\text{tot}} + \nabla p - \frac{1}{Re} \Delta \mathbf{u} \right\|_2^2 dt. \tag{B.1}$$

The reason for such a choice can be found in section 4.1 of [40]. We then consider the quasi-potential from one state (\mathbf{u}_1, p_1) to a new state (\mathbf{u}_2, p_2) :

$$V((\mathbf{u}_1, p_1), (\mathbf{u}_2, p_2)) = \inf_{T \in \mathbb{R}^+} \inf_{\substack{\mathbf{u}(0)=\mathbf{u}_1, p(0)=p_1 \\ \mathbf{u}(T)=\mathbf{u}_2, p(T)=p_2}} S_T(\mathbf{u}, p). \tag{B.2}$$

We separate the integration time T through a linear time scaling, where we define a new time variable $s = t/T \in [0, 1]$. For any given path \mathbf{u} , the optimality condition $\partial S_T / \partial T = 0$ yields an optimal integration time

$$T^2(\mathbf{u}, p) = \frac{\langle \partial_s \mathbf{u}, \partial_s \mathbf{u} \rangle_{\mathbf{x},s}}{\langle \text{NS}(\mathbf{u}, p), \text{NS}(\mathbf{u}, p) \rangle_{\mathbf{x},s}}. \tag{B.3}$$

Instead of considering the optimization problem in (B.2), we modify the problem as follows

$$S_{T^*}(\mathbf{u}^*, p^*) = \min_{\substack{\mathbf{u}(0)=\mathbf{u}_1 \\ \mathbf{u}(1)=\mathbf{u}_2}} \frac{T}{2} \langle T^{-1} \partial_s \mathbf{u} - \text{NS}(\mathbf{u}, p), T^{-1} \partial_s \mathbf{u} - \text{NS}(\mathbf{u}, p) \rangle_{\mathbf{x},s}, \tag{B.4}$$

where T is not an optimization parameter but a functional given by equation (B.3). The minimizer T^* is computed using the minimizer (\mathbf{u}^*, p^*) of problem (B.4). In [46], it was demonstrated that such a strategy works well no matter T^* is finite or infinite. Furthermore, by coupling h -adaptivity with respect to s , the optimal convergence rate was achieved for a finite element discretization.

Let \mathbf{u}_h and p_h be the numerical approximation of \mathbf{u}^* and p^* . Then the first-order variation of the action functional is

$$\delta S_T = T \langle T^{-1} \partial_s \mathbf{u}_h - \text{NS}(\mathbf{u}_h, p_h), T^{-1} \partial_s \delta \mathbf{u}_h - \widehat{\text{NS}}(\delta \mathbf{u}_h, \delta p_h) \rangle_{\mathbf{x},s}, \tag{B.5}$$

where $\widehat{\text{NS}}$ is the linear perturbation operator. The gradient $\nabla S_T(\mathbf{u}_h, p_h)$ then takes the form

$$\begin{cases} \left(\frac{\partial S_T}{\partial \mathbf{u}_{i,j}} \right)_1 = \delta S_T(\mathbf{u}_h, p_h) |_{\delta \mathbf{u}_h = \mathbf{e}_x h_i(x,y) \psi_j(s), \delta p_h = 0}, \\ \left(\frac{\partial S_T}{\partial \mathbf{u}_{i,j}} \right)_2 = \delta S_T(\mathbf{u}_h, p_h) |_{\delta \mathbf{u}_h = \mathbf{e}_y h_i(x,y) \psi_j(s), \delta p_h = 0}, \\ \frac{\partial S_T}{\partial p_{i,j}} = \delta S_T(\mathbf{u}_h, p_h) |_{\delta \mathbf{u}_h = 0, \delta p_h = h_i(x,y) \psi_j(s)}, \end{cases} \tag{B.6}$$

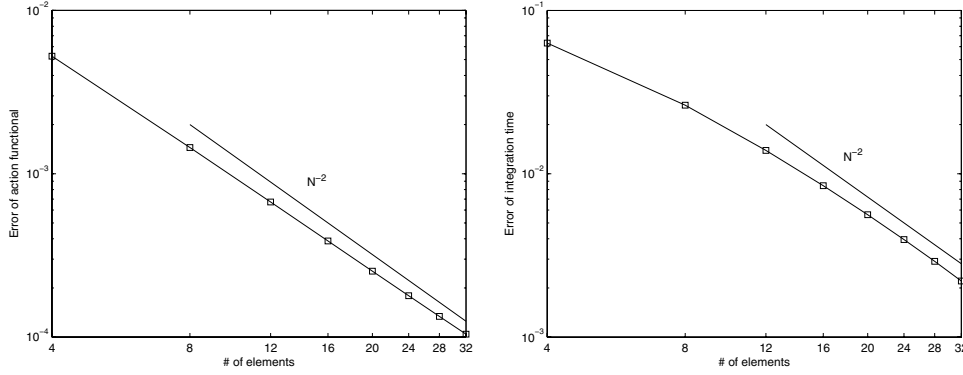


Figure B1. Left: the error of the action functional versus the number of uniform linear elements in the log-log scale. Right: the relative error ϵ_T of optimal integration time versus the number of uniform linear elements in the log-log scale.

where $\mathbf{e}_x = (1, 0)$, $\mathbf{e}_y = (0, 1)$, and $\{h_i(x, y)\}_{i=1}^{N_x}$ and $\{\psi_j(s)\}_{j=1}^{N_s}$ span the approximation space for physical and temporal discretization, respectively. Actually, the gradient takes the same form as that defined in equation (49) in [40]. The only difference is that T is not a parameter now but a functional. Furthermore, we choose the symmetric part of the second-order variation $\delta^2 S_T$ to construct a diagonal preconditioner as

$$P_{k,k} = T \langle T^{-1} \partial_s \delta \mathbf{u}_h - \widehat{\mathbf{N}}\mathbf{S}(\delta \mathbf{u}_h, \delta p_h), T^{-1} \partial_s \delta \mathbf{u}_h - \widehat{\mathbf{N}}\mathbf{S}(\delta \mathbf{u}_h, \delta p_h) \rangle_{\mathbf{x},s}, \quad (\text{B.7})$$

where $k = 1, 2, \dots, N_x N_s$. This preconditioner is the same in form as the one defined in equation (60) in [40] except that the current T is a functional. However, the second-order variation of $\delta^2 S_T$ is not the same as before because it includes a second-order term $\delta^2 T$, which is not used for the preconditioner (B.7).

To this end, the preconditioned nonlinear conjugate gradient method given in [40] can be employed to solve the optimization problem and the same parallelization strategy given in [45] can be used for parallel computing.

As a verification of the algorithm, we consider the optimization problem defined in equation (66) in [40], which uses two consecutive snapshots of the travelling wave \mathbf{u}_+ as the starting and ending point of a transition. Then the MAP should be given by the deterministic trajectory corresponding to a zero action. For this case, tMAM can also return the optimal integration time as $T(\mathbf{u}_h^*, p_h^*)$, i.e., equation (B.3). We here consider a case that the evolution time from the first snapshot to the second one is $\hat{T} = 10$. Then the error of action functional is the value of $S_T(\mathbf{u}_h^*, p_h^*)(\mathbf{u}_h^*, p_h^*)$ and the relative error for $T^* = \hat{T}$ is

$$\epsilon_T = |T(\mathbf{u}_h^*, p_h^*) - \hat{T}|/\hat{T}. \quad (\text{B.8})$$

In figure B1, the errors of action functional and integration time are plotted with respect to the number of elements, where uniform linear finite elements are used. It can be seen that the optimal convergence rate $O(N^{-2})$ is achieved for both cases.

Appendix C. A general discussion about the numerical behaviour of MAM for spatially extended systems

In this section we would like to present a general discussion to clarify the relation between MAM and the dynamic solver.

C.1. Approximation errors of the MAP.

The main numerical issue is as follows. The action along a dynamical trajectory should be equal to zero. However, the N–S operators in the action functional (15) and the dynamic solver may not be discretized in the same way, which means that the action along a numerical trajectory can be finite.

Let V_h be the approximation space for physical discretization, where the subscript h indicates numerical approximation. Then $\mathbf{u}_h \in V_h$ is a curve in the reduced phase space. For simplicity, we here use the semi-discrete form without the temporal discretization. To approximate the solution of the deterministic N–S equations, we actually solve the following semi-discrete N–S equation

$$\partial_t \mathbf{u}_h - \mathcal{P}_h \text{NS}(\mathbf{u}_h) = 0, \tag{C.1}$$

where \mathcal{P}_h indicates the projection of $\text{NS}(\mathbf{u}_h)$ onto the divergence-free space such that the equation is closed. For the numerical approximation of MAP, we minimize the following discrete action functional:

$$S_{h,T}(\mathbf{u}_h) = \frac{1}{2} \int_0^T \|\partial_t \mathbf{u}_h - \text{NS}(\mathbf{u}_h)\|_2^2 dt. \tag{C.2}$$

If \mathbf{u}_h corresponds to a trajectory given by equation (C.1) on time interval $[0, T]$, we have

$$\begin{aligned} S_{h,T}(\mathbf{u}_h) &= \frac{1}{2} \int_0^T \|\partial_t \mathbf{u}_h - \mathcal{P}_h \text{NS}(\mathbf{u}_h) + (\mathcal{I} - \mathcal{P}_h) \text{NS}(\mathbf{u}_h)\|_2^2 dt \\ &= \frac{1}{2} \int_0^T \|(\mathcal{I} - \mathcal{P}_h) \text{NS}(\mathbf{u}_h)\|_2^2 dt, \end{aligned} \tag{C.3}$$

where \mathcal{I} is an identity operator. In other words, the trajectory of system (C.1) has a nonzero action induced by numerical approximation, which goes to zero as spatial resolution is refined. We can roughly regard such a nonzero action as the approximation error of the action functional induced by the finite approximation space. It is easy to see that $\|(\mathcal{I} - \mathcal{P}_h) \text{NS}(\mathbf{u}_h)\|_2$ can be relatively large when the high-order modes of \mathbf{u}_h are important.

Another source of approximation errors for the action functional is the aliasing error. When evaluating the action functional, we need to use the Gauss quadrature rule. Note that the polynomial degree of the integrand of

$$\frac{1}{2} \int_0^T \|\text{NS}(\mathbf{u}_h)\|_2^2 dt$$

is four times as large as the polynomial degree of \mathbf{u}_h . To evaluate this term exactly we need quadrature points twice as many as the polynomial degree in each direction, i.e., t -, x - and y -direction. The computation cost will be eight times as much as the choice of the pseudo-spectral method. In this work, we choose the number of quadrature points comparable to the polynomial degree in each direction due to the demanding computation cost.

C.2. Local force and local residual.

Consider the numerical MAP $\mathbf{u}_{\mathbf{a} \rightarrow \mathbf{b}}(t)$ from one attractor \mathbf{a} to another attractor \mathbf{b} . Let us define

$$F_{\mathbf{u}_{\mathbf{a} \rightarrow \mathbf{b}}}(t, \mathbf{x}) = \partial_t \mathbf{u}_{\mathbf{a} \rightarrow \mathbf{b}} - \text{NS}(\mathbf{u}_{\mathbf{a} \rightarrow \mathbf{b}}) \tag{C.4}$$

as the local force required to achieve the transition from \mathbf{a} to \mathbf{b} . For a numerical trajectory $U_{\hat{\mathbf{u}}(\mathbf{x})}(\tau)$ the local residual is

$$R_{\hat{\mathbf{u}}(\mathbf{x})}(\tau, \mathbf{x}) = \partial_\tau U_{\hat{\mathbf{u}}(\mathbf{x})} - \text{NS}(U_{\hat{\mathbf{u}}(\mathbf{x})}), \tag{C.5}$$

which is, in general, not equal to zero since $U_{\hat{\mathbf{u}}(\mathbf{x})}$ only satisfies equation (C.1).

Then the local residual along the MAP $\mathbf{u}_{\mathbf{a} \rightarrow \mathbf{b}}(t)$ is denoted as $R_{\mathbf{u}_{\mathbf{a} \rightarrow \mathbf{b}}(t)}(\tau, \mathbf{x})$, which actually shares a similar form with $F_{\mathbf{u}_{\mathbf{a} \rightarrow \mathbf{b}}}(t, \mathbf{x})$. The fundamental difference is that the time variable t in $F_{\mathbf{u}_{\mathbf{a} \rightarrow \mathbf{b}}}(t, \mathbf{x})$ is defined by the *stochastic* Navier-Stokes equations while the time variable τ in $R_{\mathbf{u}_{\mathbf{a} \rightarrow \mathbf{b}}(t)}(\tau, \mathbf{x})$ is defined by the *deterministic* N-S equations.

Consider the MAP $\mathbf{u}_{\mathbf{a} \rightarrow \mathbf{b}}$ from attractor \mathbf{a} to attractor \mathbf{b} . A reasonable expectation is that for a certain point $\mathbf{u}_{\mathbf{a} \rightarrow \mathbf{b}}(t)$ located in the basin of attraction of \mathbf{a} , the local force $F_{\mathbf{u}_{\mathbf{a} \rightarrow \mathbf{b}}}(t, \mathbf{x})$ should be larger than the local residual $R_{\mathbf{u}_{\mathbf{a} \rightarrow \mathbf{b}}(t)}(0^+, \mathbf{x})$ for a certain t because $U_{\mathbf{u}_{\mathbf{a} \rightarrow \mathbf{b}}(t)}$ will choose a direction back to \mathbf{a} while the MAP will choose a direction to escape the domain of attraction of \mathbf{a} . If the approximation of the action functional is too coarse which cannot recognize the local residual and the external noise, we then have troubles. In other words, we need that

$$\|F_{\mathbf{u}_{\mathbf{a} \rightarrow \mathbf{b}}}(t, \mathbf{x})\|_2 \gg \|R_{\mathbf{u}_{\mathbf{a} \rightarrow \mathbf{b}}(t)}(0^+, \mathbf{x})\|_2, \tag{C.6}$$

if $\mathbf{u}_{\mathbf{a} \rightarrow \mathbf{b}}$ is located in the basin of attraction of \mathbf{a} . Note here $\|R_{\mathbf{u}_{\mathbf{a} \rightarrow \mathbf{b}}(t)}(0^+, \mathbf{x})\|_2$ is the local residual when $\tau \rightarrow 0^+$. To approximate $\|R_{\mathbf{u}_{\mathbf{a} \rightarrow \mathbf{b}}(t)}(0^+, \mathbf{x})\|_2$ at $\tau = 0^+$, we run the dynamic solver for a few time steps and take the average of $\|R_{\mathbf{u}_{\mathbf{a} \rightarrow \mathbf{b}}(t)}(0^+, \mathbf{x})\|_2$ at each moment. In this work, we usually run 10 time steps with $\Delta t = 10^{-5}$.

For the part of $\mathbf{u}_{\mathbf{a} \rightarrow \mathbf{b}}$ that is located in the basin of attraction of \mathbf{b} , we have to face the following problem: the action along a trajectory is theoretically equal to zero while numerical approximation always induces non-zero numerical residuals. For a dynamic solver, the residual is a local behaviour in time, which is consistent with the distance $U_{\hat{\mathbf{u}}}$ from the true solution of deterministic N-S equations. For the action functional, the residual becomes global due to the integration. Although the MAM can indeed recover a trajectory using $U_{\hat{\mathbf{u}}}(0)$ and $U_{\hat{\mathbf{u}}}(T)$ as the two end points [40] up to a certain accuracy, the local residuals can accumulate through the numerical integration and introduce troubles. One particular case is that the action required to escape the basin of attraction of \mathbf{a} is small while in the basin of the attraction of \mathbf{b} the dynamic solver needs a long relaxation time to converge to \mathbf{b} with a bounded but not decreasing local residual. Then in the basin of attraction of \mathbf{b} the MAM may not follow the trajectory due to the accumulated local residuals. This scenario occurs for the transitions between the stable solutions \mathbf{u}_0 and \mathbf{u}_+ of the N-S equations.

C.3. Discrepancy between the dynamical solver and the numerical action functional.

The discrepancy between the dynamical solver and the numerical action functional can be alleviated by a modification of the action functional as

$$S_{h,T}(\mathbf{u}_h) = \frac{1}{2} \int_0^T \|\partial_t \mathbf{u}_h - \mathcal{P}_h \text{NS}(\mathbf{u}_h)\|_2^2 dt, \tag{C.7}$$

which is more consistent with the dynamical solver (C.1) instead of the N-S equations. We did not use this strategy due to the following concerns: (1) we do not have a unified procedure to achieve \mathcal{P}_h for the dynamic solver and MAM. For example, the most popular dynamic solver is based on the projection method where the divergence-free constraint is satisfied implicitly. In our current MAM, the divergence-free constraint is achieved explicitly. (2) As the spatial resolution becomes fine enough, the difference between $\mathcal{P}_h \text{NS}(\mathbf{u}_h)$ and $\text{NS}(\mathbf{u}_h)$ should be very small. (3) This is our first attempt to use MAM to examine transitions in the phase space of the N-S equations. We need to know how such a discrepancy affects the numerical results.

Acknowledgments

XW was supported by NSF Grant DMS-1115632. HY was partially supported by NNSFC Grants 11101413 and 11371358. WE was partially supported by ONR Grant N00014-13-1-0338 and Major Program of NNSFC under Grant 91130005.

Reference

- [1] Heisenberg W 1924 Über stabilität und turbulenz von flüssigkeitsströmen *Ann. Phys.* **74** 577–627
- [2] Tollmien W 1929 Über die entstehung der turbulenz *Nachr. Ges. Wiss. Göttingen Math.-Phys. Kl.* 21–44
- [3] Schlichting H 1933 Berechnung der anfängung kleiner störungen bei der plattenströmung *Z. Angew. Math. Mech.* **13** 171–4
- [4] Lin C C 1955 *The Theory of Hydrodynamic Stability* (Cambridge: Cambridge University)
- [5] Drazin P G and Reid W H 1981 *Hydrodynamic Stability* (Cambridge: Cambridge University)
- [6] Orszag S A 1971 Accurate solution of the Orr–Sommerfeld stability equation *J. Fluid Mech.* **50** 689–703
- [7] Barly B J, Orszag S A and Herbert T 1988 Instability mechanisms in shear-flow transition *Ann. Rev. Fluid Mech.* **20** 359–91
- [8] Stuart J T 1960 On the non-linear mechanics of wave disturbances in stable and unstable parallel flows: I. The basic behaviour in plane Poiseuille flow *J. Fluid Mech.* **9** 353–70
- [9] Watson J 1960 On the non-linear mechanics of wave disturbances in stable and unstable parallel flows: II. The development of a solution for plane Poiseuille flow and for plane Couette flow *J. Fluid Mech.* **9** 371–89
- [10] Landau L D 1944 On the problem of turbulence *Dokl. Akad. Nauk SSSR* **44** 339–43
- [11] Reynolds W C and Potter M C 1967 Finite-amplitude instability of parallel shear flows *J. Fluid Mech.* **27** 465–92
- [12] Pekeris C L and Shkoller B 1971 Stability of plane Poiseuille flow to periodic disturbances of finite amplitude *Proc. Natl Acad. Sci. USA* **68** 197–9, 1434–5
- [13] Zahn J-P, Toomre J, Spiegel E A and Gough D O 1974 Nonlinear cellular motions in Poiseuille channel flow *J. Fluid Mech.* **64** 319–45
- [14] Herbert T 1976 *Periodic Secondary Motions in a Plane Channel* ed A I van de Vooren and P J Zandbergen (Berlin: Springer) p 235–40
- [15] Wolf L, Lavan Z and Nielsen H J 1978 Numerical computation of the stability of plane Poiseuille flow *J. Appl. Mech.* **45** 13–8
- [16] Orszag S A and Petera A T 1980 Subcritical transition to turbulence in plane channel flows *Phys. Rev. Lett.* **45** 989–93
- [17] Rozhdestvensky B L and Simakin I N 1984 Secondary flows in a plane channel: their relationship and comparison with turbulent flows *J. Fluid Mech.* **147** 261–89
- [18] Farrell B and Ioannou P 1996 Generalized stability theory: I. Autonomous operators *J. Atmos. Sci.* **53** 2025–40
- [19] Schmid P J and Henningson D S 2001 *Stability and Transition in Shear Flows* (New York: Springer)
- [20] Trefethen L and Embree M 2005 *Spectra and Pseudospectra: The Behavior of Nonnormal Matrices and Operators* (Princeton, NJ: Princeton University)
- [21] Trefethen L 1997 Pseudospectra of linear operators *SIAM Rev.* **39** 383–406
- [22] Schmid P J 2007 Nonmodal stability theory *Annu. Rev. Fluid Mech.* **39** 129–62
- [23] Joseph D D 1976 *Stability of Fluid Motions* vol 1 (New York: Springer)
- [24] Schneider T M, Gibson J F, Lagha M, De Lillo F and Eckhardt B 2008 Laminar-turbulent boundary in plane Couette flow *Phys. Rev. E* **78** 037301
- [25] Chantry M and Schneider T M 2014 Studying edge geometry in transiently turbulent shear flows *J. Fluid Mech.* **747** 506–17
- [26] Itano T and Toh S 2001 The dynamics of bursting process in wall turbulence *J. Phys. Soc. Japan* **70** 703–16
- [27] Schneider T M and Eckhardt B 2009 Edge states intermediate between laminar and turbulent dynamics in pipe flow *Phil. Trans. R. Soc. A* **367** 577–87
- [28] Mellibovsky F, Meseguer A, Schneider T M and Eckhardt B 2009 Transition in localized pipe flow turbulence *Phys. Rev. Lett.* **103** 054502
- [29] Skufca J D, Yorke J A and Eckhardt B 2006 Edge of chaos in a parallel shear flow *Phys. Rev. Lett.* **96** 174101
- [30] Cherubini S, De Palma P, Robinet J-Ch and Bottaro A 2010 Rapid path to transition via nonlinear localized optimal perturbations in a boundary-layer flow *Phys. Rev. E* **82** 066302
- [31] Pringle C C T and Kerswell R R 2010 Using nonlinear transient growth to construct the minimal seed for shear flow turbulence *Phys. Rev. Lett.* **105** 154502

- [32] Cherubini S, De Palma P, Robinet J-Ch and Bottaro A 2011 The minimal seed of turbulent transition in the boundary layer *J. Fluid Mech.* **689** 221–53
- [33] Monokrousos A, Bottaro A, Brandt L, Di Vita A and Henningson D S 2011 Nonequilibrium thermodynamics and the optimal path to turbulence in shear flows *Phys. Rev. Lett.* **106** 134502
- [34] Pringle C C T, Willis A P and Kerswell R R 2012 Minimal seeds for shear flow turbulence: using nonlinear transient growth to touch the edge of chaos *J. Fluid Mech.* **702** 415–43
- [35] Rabin S M E, Caulfield C P and Kerswell R R 2012 Triggering turbulence efficiently in plane Couette flow *J. Fluid Mech.* **712** 244–72
- [36] Kerswell R R, Pringle C C T and Willis A P 2014 An optimization approach for analysing nonlinear stability with transition to turbulence in fluids as an exemplar *Rep. Prog. Phys.* **77** 085901
- [37] W E, Zhou Z and Cheng X 2012 Subcritical bifurcation in spatially extended systems *Nonlinearity* **25** 761–79
- [38] Sritharan S S and Sundar P 2006 Large deviations for the two-dimensional Navier–Stokes equations with multiplicative noise *Stochastic Process. Appl.* **116** 1636–59
- [39] Freidlin M I and Wentzell A D 1998 *Random Perturbations of Dynamical Systems* 2nd edn (New York: Springer)
- [40] Wan X 2013 A minimum action method for small random perturbations of two-dimensional parallel flows *J. Comput. Phys.* **235** 497–514
- [41] Cerrai S and Freidlin M 2011 Approximation of quasi-potential and exit problems for multidimensional RDE's with noise *Trans. Am. Math. Soc.* **363** 3853–92
- [42] Brzeźniak Z, Cerrai S and Freidlin M 2014 Quasipotential and exit time for 2D stochastic Navier–Stokes equations by space time white noise *Probab. Theory Relat. Fields* arXiv:1401.6299
- [43] Hairer M and Weber H 2015 Large deviations for white-noise driven, nonlinear stochastic PDEs in two and three dimensions *Annales de la Faculté des Sciences de Toulouse* accepted arXiv:1404.5863
- [44] Zhou X, Ren W and W E 2008 Adaptive minimum action method for the study of rare events *J. Chem. Phys.* **128** 104111
- [45] Wan X and Lin G 2013 Hybrid parallel computing of minimum action method *Parallel Comput.* **39** 638–51
- [46] Wan X 2015 A minimum action method with optimal linear time scaling *Commun. Comput. Phys.* accepted
- [47] Cameron M K 2012 Finding the quasipotential for nongradient SDE's *Physica D* **241** 1532–50